


Colloquium: Magnetotactic bacteria: From flagellar motor to collective effects

M. Marmol^{✉,*}, E. Gachon^{✉,†} and D. Faivre[✉]

Aix-Marseille Université, CEA, CNRS, BIAM, 13115 Saint Paul-Lez-Durance, France

 (published 4 April 2024)

Magnetotactic bacteria are swimming microorganisms able to follow magnetic field lines with the help of an organelle called the magnetosome that is made of biomineralized magnetic crystals assembled in a chain. In combination with this ability, these bacteria perform active oxygen sensing to reach the oxic-anoxic transition zone, which is often located in the upper part of the sediment. From a physicist's perspective, magnetotactic bacteria can be seen at the interface between bacterial active matter and magnetic colloids, which gives them unique properties at both the individual and collective levels. In crowded media and/or when they are submitted to external flows, their motion can be efficiently driven by magnetic fields, which leads to surprising effects. In this Colloquium, the different features of magnetotactic bacteria are reviewed at every scale, from single cell to collective motion, from simple to complex environments, and by emphasizing the differences from other bacterial species or passive magnetic colloids. The Colloquium concludes with a discussion of perspectives on using magnetotactic bacteria in active magnetorheology.

DOI: [10.1103/RevModPhys.96.021001](https://doi.org/10.1103/RevModPhys.96.021001)

CONTENTS

| | |
|--|----|
| I. Introduction | 1 |
| II. Single Cell Motion | 3 |
| A. Physics of flagellar-based propulsion | 3 |
| 1. Bacterial flagellar motor | 3 |
| 2. Flagellar hydrodynamics | 4 |
| B. Motility behaviors | 5 |
| 1. Motility patterns | 5 |
| 2. Magnetotaxis | 6 |
| III. Single Cell Motion in Complex Media | 7 |
| A. Motion in porous media | 7 |
| 1. Motility in porous media | 7 |
| 2. Hydrodynamic interactions with obstacles | 8 |
| B. Transport with flow in porous media | 9 |
| 1. Transport in flow | 9 |
| 2. Interactions with obstacles in flow | 9 |
| IV. From Single to Collective: Magneto-aerotaxis | 10 |
| A. Single cell magneto-aerotaxis | 11 |
| B. Collective magneto-aerotactic motion | 11 |
| C. Control of the oxygen gradient | 12 |
| V. Collective Motion | 13 |
| A. Actuation by magnetic fields | 13 |
| 1. Bend and splay instabilities | 13 |
| 2. Self-assembly at surfaces | 13 |
| 3. Self-assembly under a rotating magnetic field | 15 |
| B. Actuation by flow and a magnetic field | 15 |
| VI. Rheology | 16 |
| A. Magnetorheology | 16 |
| 1. Magnetic stress and effective viscosity | 16 |
| 2. Odd viscosity in chiral fluids | 17 |
| B. Bacterial suspension rheology | 17 |

| | |
|--------------------------------------|----|
| C. Magnetoactive suspension rheology | 18 |
| 1. Motor-brake effect | 18 |
| 2. Magnetoactive pumping | 19 |
| VII. Outlook | 19 |
| A. Single cell motion | 19 |
| B. Complex media | 20 |
| C. Magneto-aerotaxis | 20 |
| D. Collective motion | 20 |
| E. Rheology | 20 |
| Acknowledgments | 20 |
| References | 20 |

I. INTRODUCTION

Magnetotactic bacteria (MTBs) orient in magnetic fields and are, from a physical point of view, self-propelled compass needles (Faivre and Schüler, 2008; Klumpp and Faivre, 2016; Bazylinski and Trubitsyn, 2019). Their magnetic properties are assured by a chain of a specific organelle called the magnetosome (Balkwill, Maratea, and Blakemore, 1980). Such chains can be imaged by transmission electron microscopy (TEM) (the black dots in Fig. 1). Magnetosomes are made up of magnetic biominerals such as magnetite (Frankel, Blakemore, and Wolfe, 1979) and greigite (Heywood *et al.*, 1990; Mann *et al.*, 1990) enveloped in a lipid bilayer (Gorby, Beveridge, and Blakemore, 1988).

MTBs are found in sedimentary media all over the globe and evolve in stratified environments in the oxic-anoxic transition zone (OATZ) (Lefèvre and Bazylinski, 2013). To reach the OATZ, MTBs perform a combination of passive alignment along Earth's magnetic field lines and an active mechanism of oxygen sensing called magneto-aerotaxis (Frankel *et al.*, 1997; Faivre and Schüler, 2008). To fully comprehend and model MTBs' motion in realistic conditions, their magnetic alignment, their sensing mechanism in oxygen gradients, the magnetic interactions between the cells, and the

*Also at Institut Lumière Matière, UMR5306 Université Claude Bernard Lyon 1, CNRS, Université de Lyon, Villeurbanne Cedex 69622, France.

†emilie.gachon@cea.fr

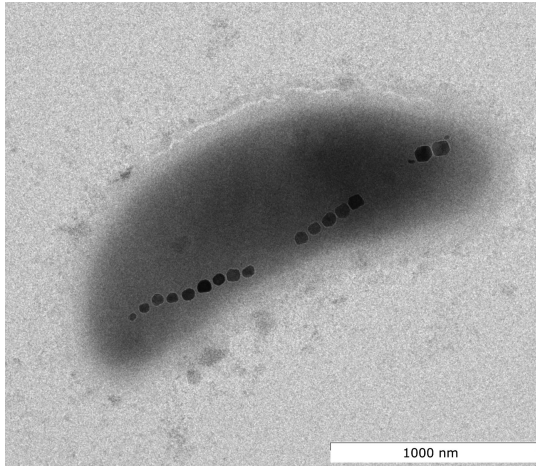


FIG. 1. TEM image of a MTB with the magnetosome chain.

hydrodynamic interactions between the cells, the porous media and the flow have to be considered.

On the one hand, MTBs belong to the bacterial active-matter world, which is a fast-growing field of research (Aranson, 2022). In addition to being self-propelled as active Brownian particles (Romanczuk *et al.*, 2012), bacteria are microswimmers (Lauga and Nadal, 2016). They are propelled by flagella, which rotate thanks to a nanoscaled motor (Berg, 2008; Xue *et al.*, 2015); this plays a key role in the study of their motion and adaptation to changes in their environment. In addition to being the driving force of MTBs' space exploration, flagellar propulsion is responsible for the hydrodynamic interactions of the cells with their environment. These are crucial when one considers MTBs' swimming behavior in the presence of an external flow (Rismani Yazdi *et al.*, 2018), in porous media (Yazdi *et al.*, 2018; Waisbord, Dehkharghani, and Guasto, 2021; Kumar, Guasto, and Ardekani, 2022), or in non-Newtonian fluids (Martinez *et al.*, 2014).

On the other hand, MTBs can be seen as magnetic colloids. This property exposes them to additional interactions compared to other bacteria, such as body forces in magnetic field gradients (Erb and Yellen, 2008; Erb *et al.*, 2008), dipole-dipole interactions (Kraftmakher, 2007), and magnetic torque (Erb *et al.*, 2016). Magnetic colloids find applications in several fields, including micromixing (Chong *et al.*, 2013), cargo delivery (Demirörs *et al.*, 2018), and hyperthermia (Perigo *et al.*, 2015).

By definition, motile active matter continuously consumes energy to produce motion. In the presence of a large amount of active particles, the movement of these particles is coupled and collective motion emerges. This is observed at the macroscale with flocking birds (Vicsek and Zafeiris, 2012; Cavagna and Giardina, 2014; Cavagna *et al.*, 2015) and schools of fish (Aoki, 1982; Calovi *et al.*, 2014; Jhavar *et al.*, 2020), and at the microscale with cytoskeleton filaments (Jlicher *et al.*, 2007; Doostmohammadi *et al.*, 2018) and microorganisms (Koch and Subramanian, 2011). Collective motion of motile active matter leads to vortices reminiscent of turbulence (Alert, Casademunt, and Joanny, 2022). This phenomenon, which is known as active turbulence, notably

differs from the classic inertial turbulence by the scale at which the energy is fed into the system.

In inertial turbulence, energy is inserted at larger scales and dissipated at smaller scales by the viscosity, while in active turbulence energy is put in by the constitutive bricks of the system. Several theoretical (Saintillan and Shelley, 2012; Bárdfalvy *et al.*, 2019; Qi *et al.*, 2022) and experimental studies (Wensink *et al.*, 2012; Gachelin *et al.*, 2014; Liu *et al.*, 2021) have shed light on the complexity of this phenomenon. Moreover, the collective motion of microorganisms is triggered and controlled by different external fields, including gravity (Bolitho, Singh, and Adhikari, 2020; Ishikawa, Dang, and Lauga, 2022), chemical fields (Hillesdon and Pedley, 1996; Kuznetsov, 2005), light (Dervaux, Resta, and Brunet, 2017; Ramamonjy, Dervaux, and Brunet, 2022; Sengupta, 2022), and flow (Jibuti *et al.*, 2014; Lauga and Nadal, 2016).

Magnetic particles also lead to impressive collective motion and self-assembled patterns (Wang, He, and Yin, 2013). Rotating magnetic fields have been widely used to produce self-assembled structures at interfaces, including hexagonal arrays of spinning disks (Grzybowski, Stone, and Whitesides, 2000), rotating crystals of Janus particles (Yan, Bae, and Granick, 2015), multisegmented patterns (Snezhko, Aranson, and Kwok, 2006), and asters (Snezhko and Aranson, 2011). Unlike bacterial collective motion, these effects take place in two dimensions because of the formation of layered structures that are promoted by magnetic interactions in rotating fields. By sharing the features of microswimmers and magnetic particles, MTBs exhibit notable collective effects and induce unique hydrodynamic instabilities.

Magnetic and active particles produce a signature in the rheological behavior of a fluid. The apparent viscosity of magnetic fluids is increased or decreased by manipulating the external magnetic field. For large enough particles of a few tens of nanometers, a constant field increases the fluid viscosity by reducing the ability of particles to rotate (McTague, 1969), while an alternating field decreases it by spinning up vortical flows (Bacri *et al.*, 1995). Moreover, particles in a rotating field induce a nondissipative term in the viscosity tensor that is known as odd viscosity (Banerjee *et al.*, 2017). Suspensions of active particles such as microswimmers change the apparent viscosity of the fluid due to the local flow induced by their swimming mechanism (Saintillan, 2018). Bacteria in a shear flow reduce the apparent viscosity and produce a “superfluidity-like” effect that is analogous to Bose-Einstein condensates in quantum matter (Gachelin *et al.*, 2013). Rheology of magnetoactive suspension is an emerging and promising field that has been investigated under a theoretical framework (Vincenti, Douarache, and Clement, 2018). MTBs could play a key role in the development of experiments on magnetoactive fluid rheology.

This introduction highlights how this Colloquium is organized from single cells to collective behaviors and from simple to more complex environments. Accordingly, in Sec. II we discuss the single cell motion of MTBs, from their propulsion mechanism and their hydrodynamic consequences to their space exploration behavior along magnetic fields. In Sec. III, we discuss the impact of complex media such as obstacles and flow on their motion. In Sec. IV, we focus on the oxygen sensing mechanism of MTBs, which has an impact at the

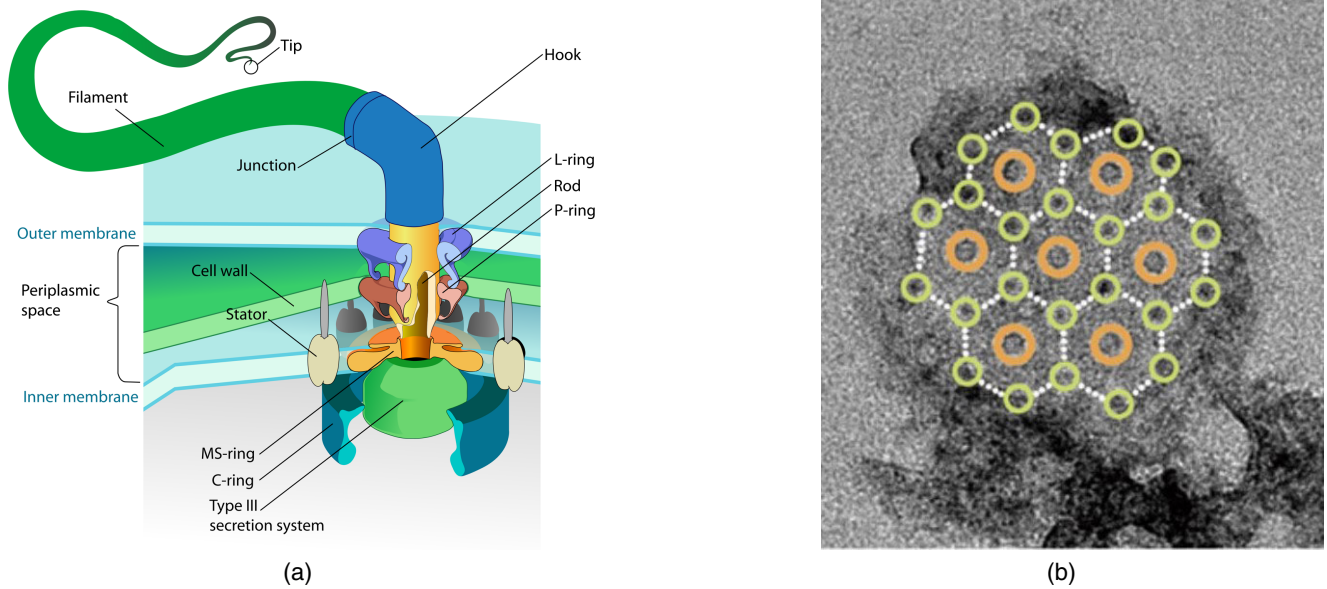


FIG. 2. (a) BFM diagram. From Mariana Ruiz Villarreal. (b) MO-1 flagellar motor architecture. The intertwined hexagonal array consists of the basal bodies of seven flagella and 24 fibrils, with large brown and small yellow-green circles overlaid on the flagellar and fibril basal bodies, respectively. From Ruan *et al.*, 2012.

single cell and collective levels. In Sec. V, we review the different types of collective motions exhibited by MTBs or magnetoactive matter. Finally, in Sec. VI we review the rheological effects brought by magnetic and active particles and highlight the potential of MTBs in future experimental studies about the rheology of magnetoactive fluids.

II. SINGLE CELL MOTION

A. Physics of flagellar-based propulsion

1. Bacterial flagellar motor

Bacteria evolve in a world free of inertia where viscous dissipation is dominant called the low Reynolds number regime. The Reynolds number, which is defined as the ratio between inertial and viscous forces, is given by

$$\text{Re} = \frac{\rho u L}{\eta}, \quad (1)$$

where ρ is the fluid density, u is the typical speed, L is the typical system length, and η is the fluid viscosity. The Reynolds number for swimming microorganisms is typically between 10^{-2} and 10^{-5} . When $\text{Re} \ll 1$, the governing equation of flow is the Stokes equation, which is linear and time reversible for steady flow, subordinated by the incompressibility condition,

$$\eta \nabla^2 \mathbf{u} - \nabla P = 0, \quad (2)$$

$$\nabla \cdot \mathbf{u} = 0. \quad (3)$$

In this regime, motion should break time symmetry to induce translation, a condition known as the scallop theorem

(Purcell, 1977; Lauga, 2016). To satisfy this constraint, MTBs propel themselves using one flagellum or several flagella, driven by a molecular rotating motor [Fig. 2(a)] (Xue *et al.*, 2015). The bacterial flagellar motor (BFM) links the flagella to the basal body via a flexible hook. The basal body, which is made of transmembrane protein rings, forms what is known as the rotor. The rotor is connected to up to a dozen stator units, each made up of four MotA and two MotB proteins. The passage of ions down the stator units induces a conformational change of the MotA proteins and provides the energy for torque generation (proton motive force) at the rotor-stator interface (Manson *et al.*, 1977). From a thermodynamics point of view, the BFM is a quasiperfect motor that works at close to 100% efficiency and reaches a rotation speed of approximately 300 Hz (Xue *et al.*, 2015). This high speed of rotation propels bacteria from $\sim 40 \mu\text{m s}^{-1}$ for *E. coli* up to $\sim 300 \mu\text{m s}^{-1}$ for some marine bacteria (Ruan *et al.*, 2012).

The marine MTB *Magnetococcus ovoid* (MO-1) is among the fastest-swimming bacteria, with a speed of about $300 \mu\text{m s}^{-1}$, and has a completely different motor organization than the most extensively studied motor of *E. coli* (Ruan *et al.*, 2012). MO-1 has two bundles of seven flagella and 24 fibrils enveloped in a sheath of glycoproteins. Their basal bodies are arranged in a hexagonal array reminiscent of the geometrical arrangement of myosin- and actin-based filaments of muscles [Fig. 2(b)]. This hexagonal architecture supposes that the fibrils counterrotate between the flagella, decreasing the friction and allowing the high-speed motion of MO-1. Note that the often studied MTB *Magnetococcus marinus* (MC-1) have the same flagellation as MO-1 and therefore should have the same motor organization. This flagellar apparatus raises questions relating to bacterial motility (see Sec. II.B.1), which have been investigated with Stokesian simulations (Bente *et al.*, 2020).

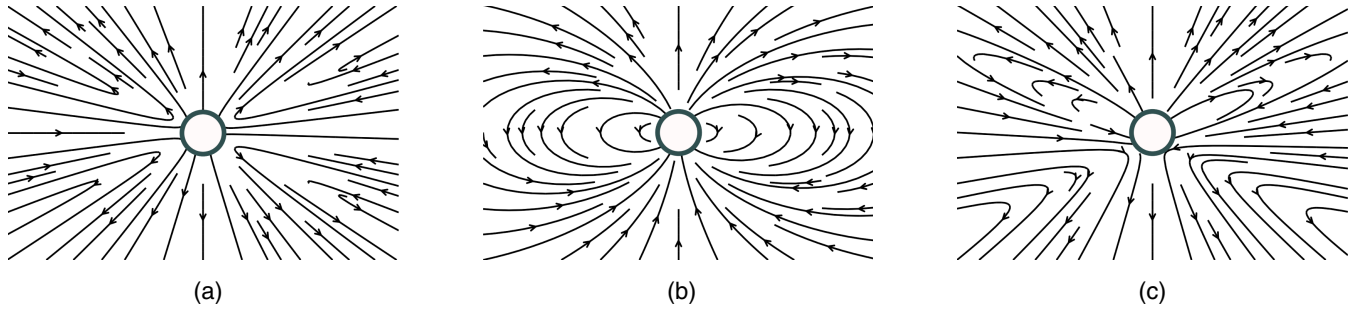


FIG. 3. Flow streamlines for (a) a force dipole of pusher type, (b) a source dipole, and (c) a force dipole plus source dipole. Data were calculated using the `PyStokes` PYTHON library (Singh and Adhikari, 2019).

2. Flagellar hydrodynamics

Swimming at a low Reynolds number implies a linear speed-force relationship such that

$$\begin{pmatrix} \mathbf{F} \\ \mathbf{T} \end{pmatrix} = \begin{pmatrix} \mathbf{A} & \mathbf{B} \\ \mathbf{B} & \mathbf{C} \end{pmatrix} \begin{pmatrix} \mathbf{v} \\ \boldsymbol{\omega} \end{pmatrix}, \quad (4)$$

where \mathbf{F} and \mathbf{T} correspond to the applied forces and torques, \mathbf{v} and $\boldsymbol{\omega}$ denote the speed and angular speed, and \mathbf{A} , \mathbf{B} , and \mathbf{C} are the submatrices of the propulsion matrix. \mathbf{A} is the translation submatrix with $A_{11} = f_{t\parallel}$ and $A_{22} = A_{33} = f_{t\perp}$. For a sphere, the friction coefficients $f_{t\parallel}$ and $f_{t\perp}$ are equal to $6\pi\eta R$, where R is the particle's radius. \mathbf{C} is the submatrix of rotation with $C_{11} = f_{r\parallel}$ and $C_{22} = C_{33} = f_{r\perp}$. For a sphere the friction coefficients $f_{r\parallel}$ and $f_{r\perp}$ are equal to $\pi\eta R^3$. The submatrix \mathbf{B} accounts for the coupling between translation and rotation and is null for a sphere. For elongated objects, the expression of the propulsion matrix is less trivial, especially for helical-shaped bodies, which are usually considered to be chains of spheres (Bahaj, James, and Moeschler, 1996) or cylinders (Nadkarni, Barkley, and Fradin, 2013). The only measurement of the propulsion matrix for helical-shaped bodies was from Yu *et al.* (2022), who used the MTB *Magnetospirillum magneticum* (AMB-1), by taking advantage of their magnetotaxis. This precise characterization of the friction coefficients has shown that slight changes in dimensions lead to drastic changes in terms of rotational friction (Yu *et al.*, 2022). In addition, for low Reynolds swimmers the estimation of the friction, and therefore of the drag force, gives access to the propulsive flagellar thrust, which for nonmagnetic strains has been measured using optical traps (Chattopadhyay *et al.*, 2006) and dielectrophoresis (Hughes and Morgan, 1999). By measuring the propulsion matrix, Yu *et al.* (2022) calculated the thrust of AMB-1 to be $\sim 0.26 \pm 0.04$ pN, which is 15 to 25 times greater than that found by Pierce *et al.* (2019) using micromagnetic traps but comparable to that of *E. coli*.

Flagellar propulsion creates flow around the bacterium, which can be seen, due to the linearity of the Stokes equation, as a sum of flow arising from different features of the cell. The reconstruction of the flow is based on a multipolar expansion of a fundamental solution of the Stokes equation called the Stokeslet, which is given by (Lisicki, 2013)

$$\mathbf{u}_{\text{Stokeslet}}(\mathbf{r}) = \mathbf{F} \cdot \mathbb{G}(\mathbf{r} - \mathbf{r}'), \quad (5)$$

where $\mathbf{F} = \delta(\mathbf{r} - \mathbf{r}')$ is the applied point force and

$$\mathbb{G}(\mathbf{r}) = \frac{1}{8\pi\eta r} \left(\mathbb{I} + \frac{\mathbf{r} \otimes \mathbf{r}}{r^2} \right) \quad (6)$$

is the Green's function. Because bacteria are force free and torque free, the Stokeslet is a forbidden solution, as it comes from a net force on the fluid. Therefore, the Green's function has to be expanded into a Taylor series to construct the multipolar contributions, as is commonly done in electrostatics. The lowest allowed contribution, called the stresslet, consists of a force dipole that accounts for the drag and expulsion of fluid. The sense of the force dipole defines whether a microswimmer is a "pusher" or a "puller." A pusher drags fluid at its front and expels fluid at its back, whereas the opposite is true for a puller. The resulting flow field for a pusher, which is shown in Fig. 3(a), is given by

$$\mathbf{u}_{\text{stresslet}}(\mathbf{r}) = \frac{\sigma_0}{8\pi\eta r^3} \left[-1 + 3 \frac{(\mathbf{r} \cdot \hat{\mathbf{e}})^2}{r^2} \right] \mathbf{r}, \quad (7)$$

where σ_0 is the force dipole strength and $\hat{\mathbf{e}}$ is the swimming direction.

Equation (7) shows that the leading term decays as r^{-2} . Supplementary contributions can be added to take into account the geometrical details of the cell. The force quadrupole term, decaying as r^{-3} , takes into account the asymmetry of the body and the length of the flagella. The body's counterrotation with respect to the flagella leads to a term called the rotlet dipole also decaying as r^{-3} , which comes from a doublet with opposing point torques. The translation of the cell breaks the symmetry of the flow induced by the force dipole and leads to a source dipole term decaying as r^{-4} that appears to be a source of fluid at the front and a sink at the back the cell [Fig. 3(b)]. The combination of these two terms is shown in Fig. 3. The flow field around a swimming cell has been measured experimentally for puller algae such as *Volvox* or pusher bacteria like *E. coli*, using particle imaging velocimetry (Drescher *et al.*, 2010, 2011). Repeating these measurements with differently flagellated bacteria could shed light on the link between the flagellar apparatus and the hydrodynamics.

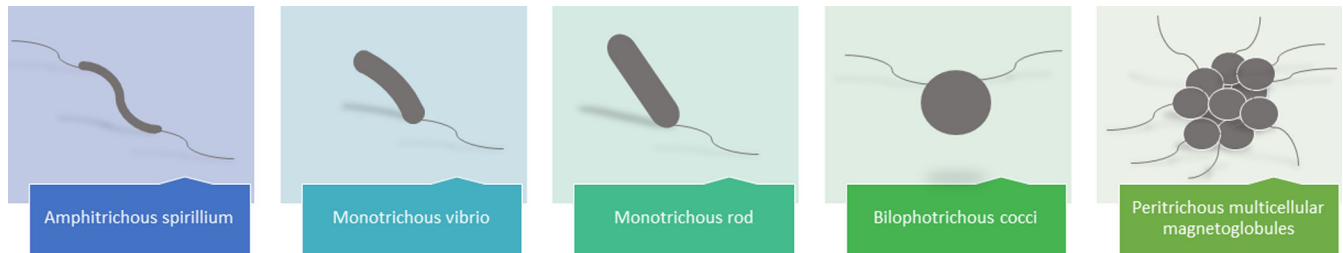


FIG. 4. The main morphologies and flagellar apparatus of MTBs (scale differences are not respected).

B. Motility behaviors

1. Motility patterns

Features of the flagellar apparatus and the morphology of the cell body itself are intimately linked to cell motility. MTBs present great diversity in terms of morphology and flagellar apparatus, from amphitrichous spirillum, monotrichous rod or vibrio, or bilophotrichous cocci with two bundles of seven flagella at one side, as well as peritrichous multicellular magnetoglobules with tens of thousands of flagella (Lefèvre *et al.*, 2014; Zhang and Wu, 2020), as shown in Fig. 4. The plurality of flagellar apparatus leads to different swimming behaviors. These behaviors are characterized by changes in swimming direction due to changes in the BFM's direction of rotation [either clockwise (CW) or counterclockwise (CCW)] directly linked to the physical and chemical sensing mechanisms of bacteria. This tuning of the swimming direction in response to external stimuli called taxis is used by microorganisms to search for nutrients (chemotaxis) (Stock and Baker, 2009), a precise amount of oxygen (aerotaxis) (Faivre and Schüler, 2008), or light (phototaxis) (Chen, Ma *et al.*, 2011).

Thus far three main patterns of motility have been described: run tumble, run reverse, and run reverse flick (Grognot and Taute, 2021). The run and tumble motility has nuances with pauses and desynchronization. This process is the one used by *E. coli* and is made up of consecutive motion in straight lines (runs) and short events of reorientation in any direction (tumbles). This motility pattern is also used by MC-1, and a study done by Waisbord *et al.* (2016b) suggested that it could be triggered, notably, by a lack of nutrients. Statistically both running and tumbling times follow a Poisson's distribution $P(\tau) = (1/\tau_c)e^{-\tau/\tau_c}$ with a characteristic timescale of $\tau_c = 1$ s for run times and 0.1 s for tumbling times (Saragosti, Silberzan, and Buguin, 2012). However, like most marine bacteria with polar flagella, MTBs often move in runs and “reversals,” where the cell moves in the opposite direction. The transition from a run to a reversal is sometimes punctuated by a turning event called a flick due to buckling of the motor hook (Son, Guasto, and Stocker, 2013).

Bacteria with polar flagella have also been shown to wrap their flagella around the cell body, which could be interpreted, in part, as an escape technique from surfaces (Kuhn *et al.*, 2017; Park *et al.*, 2022). This wrapped state results from the transition from CCW to CW rotation of the BFM and leads to motion directed toward the pole with the wrapped flagella. In the case of MTBs with a single polar flagella, this wrapped state leads to a pulling of the cell body. This push-pull-wrap

behavior has been studied using fluorescent labeling of the flagella for the lophotrichous (multiple flagella at one pole) *Pseudomonas putida* (Hintsche *et al.*, 2017) and the amphitrichous (one flagellum at each pole) MTB AMB-1 (Murat *et al.*, 2015). In both cases, the bacteria spend more time in the pushing state than in the pulling state with a wrapped flagella, but the changes in hydrodynamic behavior during this push-pull transition have yet to be explored. Unlike *Magnetospirillum magneticum* AMB-1, which tends to swim more in the pushing mode, *Magnetococcus marinus* MC-1, which has two flagella bundles at one pole, seems to swim with synergistic pushing from one bundle and pulling from the second flagella bundle (Bente *et al.*, 2020). This ability to use the two flagella bundles simultaneously along with the optimized flagellar organization within the bundles (see Sec. II.A.1) might explain the measured speed differences between these two strains ($\sim 40 \mu\text{m s}^{-1}$ for AMB-1 versus $\sim 400 \mu\text{m s}^{-1}$ for MC-1). Note that this synchronization of flagellar bundles has been experimentally investigated through high-speed dark-field microscopy imaging of MC-1's flagella and hooks and through Stokesian simulations (Bente *et al.*, 2020).

Motility leads to 3D movements, which are difficult to study in the z direction using a basic glass slide and coverslip setup. Bacteria are tracked using techniques with different natures based on 2D static tracking algorithms (Tay *et al.*, 2018), holography (Bianchi, Saglimbeni, and Di Leonardo, 2017), or moving stage techniques (Mankiewicz and Martel, 2007). Two-dimensional tracking allows for a high yield, as many bacteria are tracked simultaneously. Either the bacteria in this case are studied in thin chambers that restrict the bacteria's movement to two dimensions or the projection of their three-dimensional trajectory is used to calculate the bacteria's speed, hence leading to underestimated values. Note that hydrodynamic interactions with walls in confined geometries are stronger and tend to screen the interactions between cells. Holography, however, offers both a high yield and tracking of the bacterial trajectories in three dimensions but is difficult to implement for microswimmers whose geometry is not spherical or rod shaped. The holograms produced by the microswimmers have to be compared to simulated theoretical holograms. The cell-to-cell diversity in shape and size hence become a limiting factor for this technique. Lagrangian tracking with an automated moving stage is particularly useful for tracking bacteria over several minutes and quantifying the different diffusion behaviors that might arise over long time-scales. Moreover, fluorescence microscopy with a labeled bacterial body, flagella, or both can be coupled to this

technique to increase the accuracy of the motility study (Darnige *et al.*, 2017); however, statistics are low, as only a single microswimmer is tracked at a time.

2. Magnetotaxis

MTBs are aquatic bacteria that thrive in low oxygen concentration environments. They biomineralize iron nanoparticles encapsulated in a lipid bilayer that forms an organelle known as the magnetosome: chains. The magnetosome magnetic crystal can be made of iron oxide (magnetite), iron sulfide (greigite), or both, depending on the bacterial strain (Heywood *et al.*, 1990). The size of the nanoparticles is crucial for the magnetic properties of the material. For a magnetite nanoparticle below 30 nm, the magnetic phase is superparamagnetic because thermal fluctuations are strong enough to randomly flip the magnetization. Between 30 and 80 nm, the phase is ferrimagnetic with a single domain and is multidomain beyond 80 nm. Typical magnetosome crystals are in the range of 30–120 nm, which provides them with a permanent magnetic moment (Klumpp *et al.*, 2019). However, it is the alignment of the crystals along the filament that provides a sufficient magnetic moment to align the cells along Earth's field lines. Moreover, although the magnetic phase of the crystals is ferrimagnetic, a suspension of MTBs is considered paramagnetic because an external magnetic field is necessary to obtain a global alignment of the cells (Nadkarni, Barkley, and Fradin, 2013). Thus, the Langevin paramagnetic model can be applied to the study of the magnetization of the system.

The alignment of a bacterium to a magnetic field requires an energy E of

$$E = -mB \cos(\theta), \quad (8)$$

where B is the magnetic field, m is the MTB's magnetic moment, θ is the angle between the directions of the two, and $k_B T$ corresponds to the thermal energy, where k_B is the Boltzmann constant and T is the temperature. For a room

temperature of 25 °C, $k_B T = 4.16 \times 10^{-21}$ J. Alignment of a MTB to Earth's magnetic field, which has a magnitude of 50 μ T, requires the magnetic moment of a MTB to be at least equal to 8×10^{-17} A m². The average magnetic moment of MTBs has been measured using various experimental techniques ranging from holographic measurements in the transmission electron microscope to optical tweezer experiments and trajectory analysis of MTBs performing U turns under the switching of the direction of a magnetic field, all of which have yielded magnetic moments greater than 1×10^{-16} A m². Hence, Earth's magnetic field is sufficient to passively align the bacteria against thermal fluctuations. Considering a MTB as a paramagnetic system leads to an orientation statistics that follows a Boltzmann distribution,

$$p(\theta) = \frac{1}{Z} e^{(mB_{\text{ext}}/k_B T) \cos(\theta)}, \quad (9)$$

where Z is the partition function, m is the magnetic moment, B_{ext} is the external magnetic field, and θ is the angle between the field and the magnetic moment.

The average of the cosine of the angle θ is given by the so-called Langevin function, which is shown in Fig. 5(a) and defined as

$$\langle \cos(\theta) \rangle = \coth\left(\frac{mB_{\text{ext}}}{k_B T}\right) - \frac{k_B T}{mB_{\text{ext}}}. \quad (10)$$

For strictly two-dimensional motion in the focal plane, where θ is the projected angle along the optical axis, the angle distribution is

$$p_{2D} = \frac{e^{(mB_{\text{ext}}/k_B T) \cos(\theta)}}{2\pi I_0(mB_{\text{ext}}/k_B T)}. \quad (11)$$

While in the 3D case

$$p_{3D} = \frac{I_1[(mB_{\text{ext}}/k_B T) \cos\theta] + L_{-1}[(mB_{\text{ext}}/k_B T) \cos\theta]}{4(k_B T/mB_{\text{ext}}) \sinh(mB_{\text{ext}}/k_B T)}, \quad (12)$$

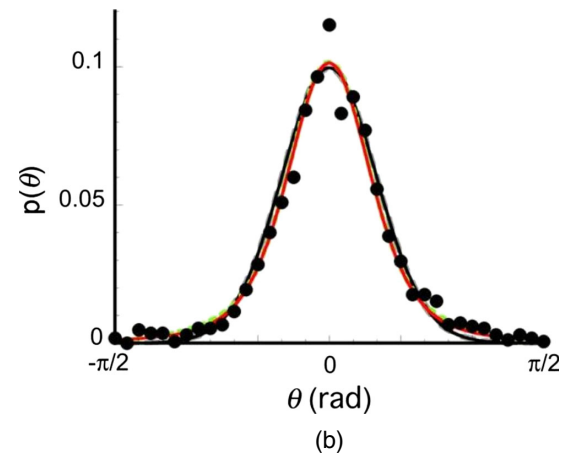
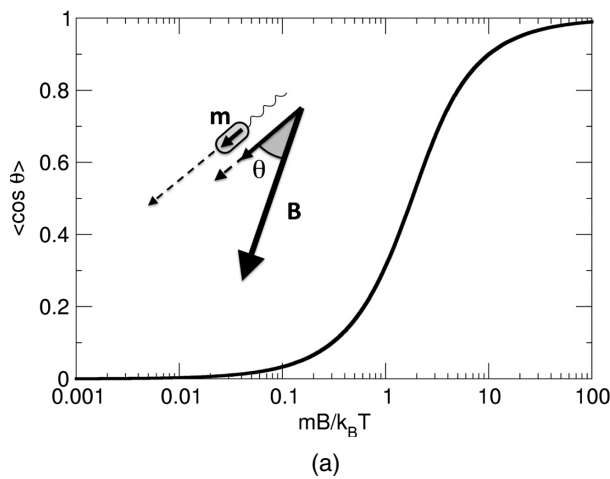


FIG. 5. (a) The average of the cosine of the angle between m , the magnetic moment, and the external field is given by the Langevin function and corresponds to the paramagnetic model. (b) The experimental orientation distribution of the magnetic moment of MTBs measured with an external field of $B = 0.3$ mT and fitted with Eq. (9) for $T = 300$ K. From Nadkarni, Barkley, and Fradin, 2013, and Klumpp *et al.*, 2019.

where I_n and L_n are the modified Bessel and Struve functions of the first kind and order n . An example of an experimental orientation distribution of MTBs' magnetic moments fitted by Eq. (9) is shown in Fig. 5(b).

When considering the mechanics, one describes the motion of MTBs using the following stochastic Langevin equations:

$$\dot{\vec{r}} = v_b \vec{e} + \sqrt{2D_t} \vec{\xi}_t, \quad (13)$$

$$\dot{\vec{e}} = -\frac{1}{\gamma_r} m B_{\text{ext}} \sin(\alpha) + \sqrt{2D_r} \vec{\xi}_r, \quad (14)$$

where v_b is the bacterial velocity, \vec{e} is the bacterial orientation, γ_r is a rotational friction coefficient, and $\xi_{t,r}$ are Gaussian translational and rotational noises with strengths given by the translational and rotational diffusion coefficients D_t and D_r . MTB motion is thus seen as an active Brownian particle submitted to a magnetic torque. Using Eqs. (13) and (14), one measures the magnetic moment of a MTB using either the reversal of the direction of a magnetic field (Acosta-Avalos *et al.*, 2019) or a rotating magnetic field (Ērglis *et al.*, 2007), both of which induce a ‘‘U turn’’ of the bacterial trajectories. When one considers the cell body as a sphere, the duration of the reversal from which the magnetic moment is calculated is given by

$$\tau = \frac{8\pi\eta R^3}{mB_{\text{ext}}} \ln\left(\frac{2mB_{\text{ext}}}{k_B T}\right). \quad (15)$$

Bear in mind that some MTBs show a misalignment between the cell and the dipole axis that interferes with their motion along magnetic fields (Nagard *et al.*, 2019). Although they are considered a paramagnetic material, the activity of the bacteria induces deviations from this model due to nonthermal noise contributions stemming from the cell reorientation (Nadkarni, Barkley, and Fradin, 2013; Taukulis and Cebers, 2014). This excess of noise is usually explained by an effective temperature of the system that does not perfectly match the rotational diffusion coefficient of the cell. Similarly, a correlated internal noise defined as $(\sqrt{D_c/\tau})\eta_c$ has been considered, where η_c corresponds to colored noise, characterized by a correlation time τ , which affects the translational and rotational diffusion (Smyk *et al.*, 2021). Nevertheless, motility patterns such as reversals, flicks, and tumbling are not considered here. Those motility patterns are, however, crucial in the limitations of the paramagnetic description of MTBs. It has been shown in the case of tumbling MTBs that the orientation distribution with respect to the field diverges above a certain critical magnetic field, a phenomenon called velocity condensation (Rupprecht *et al.*, 2016). This divergence is required to explain the high directional response of running and tumbling magnetotactic bacteria, even when they are perturbed by a Gaussian rotational noise.

III. SINGLE CELL MOTION IN COMPLEX MEDIA

MTBs are ubiquitous and are noticeably found in sedimentary media (Lefèvre and Bazylinski, 2013), which raises the issue of their diffusion in porous media instead of bulk

liquid media. Moreover, for medical applications they are expected to swim in blood vessels, which in addition to being crowded are submitted to strong flows of non-Newtonian fluid (Alphandry, 2020). We discuss in this section the behavior of MTBs in porous media in terms of diffusion, hydrodynamic interactions with obstacles, and coupling with an external flow.

A. Motion in porous media

1. Motility in porous media

Diffusivity and motility patterns of swimming microorganisms are affected by the geometrical constraints of their environment. Regarding the density, the shape, the order, and the dimensions of these constraints, different diffusion behaviors occur (Martínez-Calvo, Trenado-Yuste, and Datta, 2021). Raatz *et al.* (2015) showed that, in a two-dimensional network of ordered cylindrical pillars, the diffusion of polar bacteria is affected by the mean free path length between the obstacles. If the mean free path length is larger than the mean run length of the bacteria, the trajectory is not influenced by the collisions with the obstacles. Surprisingly when the interobstacle free space is reduced to about the size of the bacteria, the diffusion becomes more ballistic and the turning angle distribution (the angle between the two runs) shows a peak at 90° resulting from collisions with the pillars. In the crystalline regime of obstacle packing, the movement of *E. coli* is simplified to long straight runs, while active Janus particles are trapped in orbital trajectories (Brown *et al.*, 2016). This difference in behavior is attributed to the interaction between the flagella and the obstacles, which might hinder *E. coli*'s ability to deviate from a straight path. In two-dimensional porous media of random lattices, space exploration, on the contrary, is reduced and is marked by transient subdiffusion (Morin *et al.*, 2017; Sosa-Hernández, Santillán, and Santana-Solano, 2017).

Magnetotaxis amplifies the changes of diffusive behavior in porous media. In a two-dimensional ordered array of hexagonal obstacles, MTBs have a straight trajectory while submitted to a magnetic field, which enhances their migration (Fig. 6) (Yazdi *et al.*, 2018). Both nonmagnetic bacteria and field-directed MTBs' swimming speeds increase when the volume fraction of obstacles is increased. The efficiency of the migration, however, is dependent on the magnetic field strength. Simulated trajectories of MTBs in a 2D array of disordered pillars showed that the optimal field strength for net displacement is about that of Earth (Cerdá-Doñate, 2020). When the field is 10 times greater, MTBs get stuck on obstacles and diffusion is lowered.

Although providing insights into bacterial motility in porous media, 2D space exploration is not sufficient to fully account for bacterial transport. A study of the 3D motion of *E. coli* in jammed hydrogels recently showed the necessity of a change of paradigm in the description of their motility patterns (Bhattacharjee and Datta, 2019a). Instead of performing patterns of ‘‘run and tumbles,’’ bacteria performed ‘‘hops and traps’’ consisting of truncated runs and transient trapping. While trapped, the cell body continues to rotate and reorient itself until the bacteria successfully escape (Perez *et al.*, 2021).

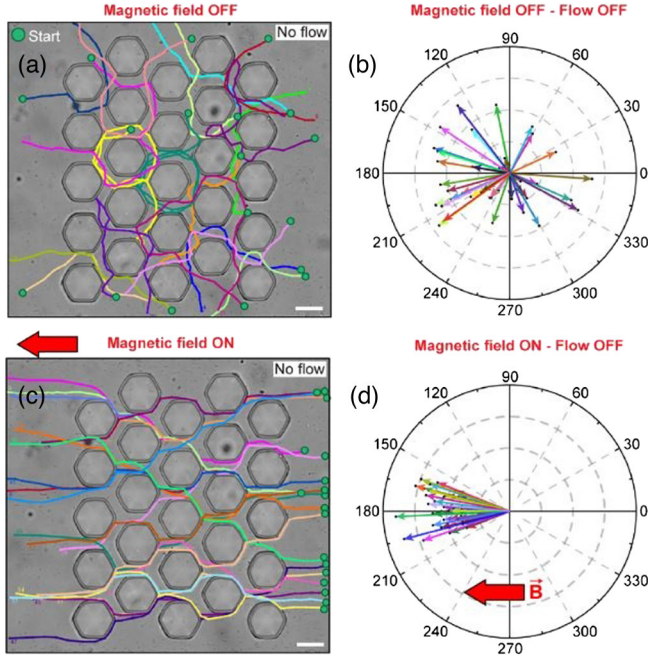


FIG. 6. Swimming trajectories of MTBs through a homogeneous porous micromodel (a) in the absence of and (b) in the presence of an applied magnetic field of 0.3 mT, with the corresponding polar graphs of progressive velocities overlaid in the center in (c) and (d). From Yazdi *et al.*, 2018.

While hop lengths are defined by the confinement, the trapping duration depends on the activity of the bacteria (Bhattacharjee and Datta, 2019b). An entropy-based model was proposed to describe the trapped state by considering that traps lower the number of available physical states that the bacteria can be in. Investigating this paradigm of motion in 3D porous media with MTBs is the next step toward understating their motion along magnetic fields in complex situations.

2. Hydrodynamic interactions with obstacles

In addition to space congestion, obstacles and surfaces induce hydrodynamic interactions with microswimmers. To satisfy the no-slip boundary condition of the flow created by a microswimmer, it is common to consider a virtual microswimmer of the same type inside the wall acting as a mirror image (Lauga, 2016). The flow created by this mirror image consists of a force dipole, a force quadrupole, and a source dipole and induces a positioning of the cell body with respect to the surface that is dependent on the swimmer type. The vorticity thus generated at the point \vec{r} is given by

$$\vec{\Omega}(\vec{r}) = \vec{\nabla} \times \vec{u} = \frac{3p}{4\pi\eta} \frac{(\vec{e} \cdot \vec{r})(\vec{e} \times \vec{r})}{r^5}. \quad (16)$$

The stable state that minimizes the vorticity is therefore parallel to the surface for pushers and orthogonal for pullers. Hydrodynamic interactions with flat surfaces also induce a trapping circular motion (Elgeti and Gompper, 2016). Because microswimmers are torque free, the body, which counter-rotates with respect to the flagella, experiences a wall-induced force in the opposite direction of the flagella, leading to a

circular motion. The sense of this motion depends on the type of swimmer, the chirality of the flagellum, and the slip condition at the surface. The hydrodynamic interactions of magnetotactic bacteria with surfaces can be tuned with the magnetic field (Pierce *et al.*, 2017). For the polar flagellated MTBs, an in-plane magnetic field stabilizes the motion along the surface by adding a magnetic torque in addition to the hydrodynamic torque. For an orthogonal field, a competition between the magnetic and the hydrodynamic torque arises, leading to “toplike” states when the magnetism dominates or “orbitlike” states when the hydrodynamic interactions dominate [Fig. 7(a)]. The critical magnetic field that separates the two states is given by

$$B_c = \frac{f'_r v_b}{m L}, \quad (17)$$

where f'_r is the out-of-plane rotational drag coefficient and L is the MTB length, with a typical value $B_c \simeq 5$ mT. In the toplike state, MTBs, which are facing a flat obstacle, easily escape by performing run and reverses without being hydrodynamically trapped (Yazdi *et al.*, 2018). When the field direction is oblique to the surface, the bacteria swim in the direction of the field against the surface due to the reduction of the flagellar drag [Fig. 7(e)] (Pierce *et al.*, 2017). For strong oblique magnetic fields and a height confinement of $10 \mu\text{m}$, a parallelogram-shaped looping motion between the top and bottom walls is observed (Yazdi *et al.*, 2018).

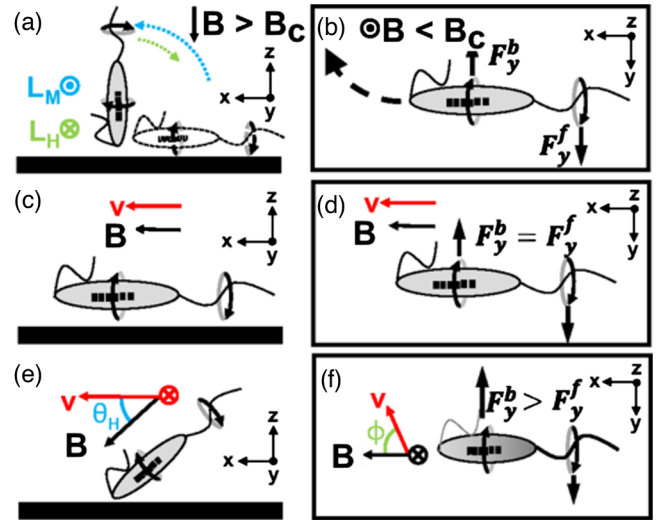


FIG. 7. (a) Competition between the hydrodynamic (L_H) and magnetic (L_M) torques controls the transitions between the toplike states (the body in the solid line) and orbitlike states (the body in the dashed line) when the field \mathbf{B} is oriented perpendicularly to the surface. (b) Rolling forces on the cell body F_y^b and the flagellum F_y^f lead to circular swimming of the bacteria at the surface. (c),(d) Cell swimming under the purely in-plane field B_x , where $F_y^b = F_y^f$. (e),(f) Cell oriented at an angle θ_H relative to the surface. (f) As the cell is tilted out of plane, F_y^f is attenuated, yielding an unbalanced hydrodynamic force in the y direction, causing the bacterium to swim toward the left of the image. From Pierce *et al.*, 2017.

Curved walls also trap microswimmers. Experiments with *E. coli* showed that trapping occurs with convex pillars (Sipos *et al.*, 2015) with an efficiency that is greatly reduced below a critical curvature radius $R^* \sim 2l/3[\sin(\theta_\infty)]$, where l is the flagellar bundle length and θ_∞ is the swimming angle against a surface with an infinite curvature radius. For *E. coli*, this radius is about 50 μm . As for flat obstacles, magnetic fields hinder the hydrodynamic interactions near curved walls and help the MTBs to escape. For convex pillars, MTBs escape from the vicinity of the pillars when their swimming direction matches the field direction if their magnetic torque overcomes the hydrodynamic torque (Yazdi *et al.*, 2018). For concave circular microfluidic traps, MTBs follow the curvature of the wall when no magnetic field is applied (Codutti *et al.*, 2022). For a strong magnetic field of 500 μT and a moderate swimming speed of 50 $\mu\text{m s}^{-1}$, the bacteria move away from the surfaces and perform U turns toward the interior of the trap. However, for the same applied field but faster bacteria the magnetic torque generated is not strong enough and bacteria still follow the curvature of the wall.

B. Transport with flow in porous media

1. Transport in flow

Transport of passive particles in a low Reynolds number flow is described using the Taylor-Aris dispersion, which results from a competition between transverse diffusion and longitudinal dispersion. For short timescales the shear gradient enhances the longitudinal dispersion, while on longer timescales diffusion redisperses the particles in the transverse direction (Taylor, 1953). The effective diffusion coefficient of the particles is written as $D_{\text{eff}} = D(1 + \text{Pe}_t^2/48)$, where Pe_t is the translational Péclet number given by $\text{Pe}_t = LU/D_r$. The Péclet number quantifies the ratio of advection over translational diffusion. In the case of elongated particles, the Taylor-Aris dispersion depends strongly on the rotational Péclet number $\text{Pe}_r = U/LD_r$ (Kumar *et al.*, 2021). Elongated particles in a flow for low Pe_r behave as spheres but tend to align with the flow direction when Pe_r increases.

In addition to the Taylor-Aris dispersion, swimming particles such as bacteria are actively propelled, adding another layer of complexity to their motion. They exhibit families of trajectories called Jeffery orbits (Jeffery and Filon, 1922; Bretherton, 1962) that are described by an active version of the Bretherton-Jeffery model. When one considers self-propulsion (Clement *et al.*, 2016),

$$\frac{d\mathbf{e}}{dt} = [\mathbf{I} - \mathbf{e} \cdot \mathbf{e}] \cdot [\beta\mathbf{E} + \Omega] \cdot \mathbf{e}, \quad (18)$$

where $\beta = (a^2 - 1)/(a^2 + 1)$ is the Bretherton parameter an aspect ratio a , \mathbf{E} is the strain-rate tensor, and Ω is the rotation-rate tensor. This model is in good agreement for a nontumbling but active bacteria (Junot *et al.*, 2019) and predicts periodic orbits that depend on the aspect ratio of the bacteria and the shear rate $\dot{\gamma}$, which is given by $T = 2\pi(r + 1/r)/\dot{\gamma}$. Adding the hydrodynamic signature of pushers or pullers near surfaces leads to a theoretical prediction in which pullers are oriented upstream, while pushers

are oscillating around the centerline (Zöttl and Stark, 2012). Near a surface, bacteria also undergo “rheotaxis,” which reorients the cell body orthogonally to the direction of the flow due to the body’s asymmetry. Depending on the shear rate, different regimes of motion can occur and can lead to upstream swimming (Mathijssen *et al.*, 2019).

Guided by a magnetic field, MTBs swim upstream and orthogonal to the flow while *E. coli* is swept away, thanks to the magnetic torque, which keeps the body aligned with the field direction (Yazdi *et al.*, 2018). The MTB *Magnetospirillum gryphiswaldense* MSR-1 is able to overcome a flow velocity that is 2 times greater while swimming in the orthogonal direction of the flow than when swimming upstream because of the difference in the experienced drag. In addition to upstream swimming, a magnetic field in the opposite direction of the flow can induce a focusing of the MTB at the center of the channel (Waisbord *et al.*, 2016a). In this situation, the equation of the torque balance is considered an Ornstein-Uhlenbeck process (Uhlenbeck and Ornstein, 1930) in which the hydrodynamic torque acts as the harmonic potential

$$mB_{\text{ext}} \frac{\dot{x}}{V_{\text{swim}}} + \frac{Kx}{w} + \zeta = 0, \quad (19)$$

where V_{swim} is the swimming speed and K is the hydrodynamic torque given by $K = \gamma_r V_{\text{flow}}/w$, with V_{flow} the flow speed, w the channel width, and ζ a random torque defined by $\zeta(t)\zeta(t') = \xi^2\delta(t - t')$. For small flows and magnetic fields, Eq. (19) leads to a Gaussian transverse density distribution of bacteria given by

$$d(x) \sim e^{-x^2/2l^2}, \quad (20)$$

where l is a width defined by $l = w\sqrt{V_{\text{swim}}B_c/V_{\text{flow}}B}$, with B_c a characteristic field given by $B_c = \xi^2/2\gamma_r m$. For stronger magnetic fields and flows, nonlinear effects occur that lead to hydrodynamic instabilities; see Sec. V.B. When the channel is inclined, the density profile is displaced to the equilibrium position given by

$$x_{\text{eq}} = w \frac{mB_{\text{ext}}}{K} \sin(\theta_{\text{mis}}), \quad (21)$$

where θ_{mis} is the misalignment angle between the horizontal direction and the channel. Compared to nonmagnetic strains, a suspension of MTBs offers additional degrees of control over the transverse dispersion of the bacteria by playing on the magnetic field and the inclination of the channel. Similar studies implying nonliving magnetic micro-objects have also shown the possibility of focusing and sorting the particles by their shape and size (Matsunaga *et al.*, 2017, 2018).

2. Interactions with obstacles in flow

The couplings among flow, obstacles, and bacterial transport lead to nontrivial effects in which bacteria explore space in a completely different way than passive particles. The no-slip condition at the surface of pillars induces a velocity gradient of the flow that leads to a hydrodynamic torque that

reorients the bacteria toward the pillar (Secchi *et al.*, 2020). While passive particles are captured at the windward side, motile bacteria are captured at the opposite side. For triangular pillar geometries, the adhesion site is on the windward side, as it captures particles more efficiently (Alonso-Matilla, Chakrabarti, and Saintillan, 2019). The adhesion efficiency does not depend on the pillar size for moderate flows but tends to decrease when the pillar diameter increases. In a porous lattice of several pillars, motility increases the transverse exploration process and leads to a non-Gaussian distribution of the longitudinal displacement with respect to the flow direction (Creppy *et al.*, 2019). Trapping phenomenon by the pillars, orthogonal counterflow swimming, and adherence to the fastest streamlines are responsible for the changes in the transport property of bacteria in a porous media with flow. In a periodic lattice, this can lead to bacterial filamentous structures attached to the pillars, depending on the angle between the flow and the lattice (Dehkharghani *et al.*, 2019). Moreover, the reduction of the transversal bacterial dispersion and enhancement of the longitudinal transport leads to a large active Taylor-Aris dispersion, with a longitudinal diffusion coefficient scaling as $D_{\parallel} \sim Pe_r^4$ instead of $D_{\parallel} \sim Pe_r^2$.

Depending on the applied magnetic field, magnetotaxis can be helpful for traveling through porous media. Even when submitted to a counterdirectional flow of $29 \mu\text{m s}^{-1}$ that normally advects *Magnetospirillum gryphiswaldense* MSR-1 bacteria in the absence of a magnetic field, they efficiently cross an array of obstacles with a porosity ranging from 0.4 to 0.6, which is relevant to the conditions found in sand sediment (Nimmo, 2004; Minagawa *et al.*, 2008), with a speed of about $25 \mu\text{m s}^{-1}$ (Yazdi *et al.*, 2018). However, in corrugated channels with counterflow different regimes of transport are observed, depending on the ratio between bacterial speed and flow speed, for a given magnetic field (Fig. 8) (Waisbord, Dehkharghani, and Guasto, 2021). These three regimes are comparable to those found for an electric diode, i.e., forward, backward, and breakdown. For a low ratio between flow and bacterial speed, transport is directed against the flow without advection, for an intermediate ratio transport is hindered and bacteria are advected near the constriction while being pushed downstream for a higher ratio. The same regimes have been identified for a network of disordered pillars where the space between the pillars acts as a congestion.

IV. FROM SINGLE TO COLLECTIVE: MAGNETO-AEROTAXIS

In most cases, MTBs prefer living in the stratified oxico-anoxic zone that corresponds to the bottom of the water column and the top of the sediment layer. The presence of sediment is crucial to the stability of the microaerophilic environments because it prevents the homogenization of the oxygen content of the water column through vertical mixing (Jørgensen and Revsbech, 1985; Brune, Frenzel, and Cypionka, 2000). This also contributes to shielding the bacteria from currents. Some magnetotactic cocci, however, have also been found in the Black Sea, where the OATZ is in the free water zone (Schulz-Vogt *et al.*, 2019).

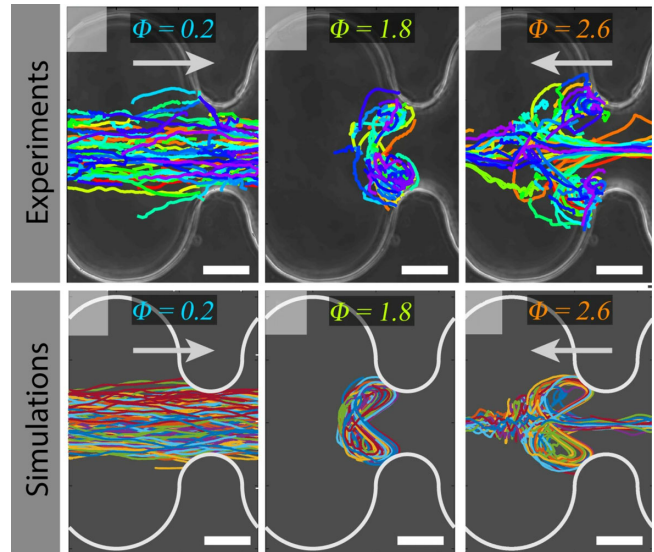


FIG. 8. Top row: experimentally measured cell trajectories in a corrugated channel with counterflow. The gray arrows indicate the direction of the bacterial transport. The scale bar = $40 \mu\text{m}$. Bottom row: Langevin simulations. Φ is the ratio between the maximum flow speed and the bacterial swimming speed (Waisbord, Dehkharghani, and Guasto, 2021).

The specifics of the MTBs' aquatic environment give a hint to the point of aligning with Earth's magnetic field. Earth's magnetic field in the Northern Hemisphere contains a vertical component that points downward. As shown in Sec. II.B.2, Earth's magnetic field is strong enough to align the bacteria with its field lines, hence reducing the bacteria's random three-dimensional search for the ideal habitat to a one-dimensional one down the water column and along an oxygen gradient (Fig. 9). Magnetotaxis is the term describing this phenomenon, which allows bacteria to navigate their environment along field lines. To date there is no concrete evidence of

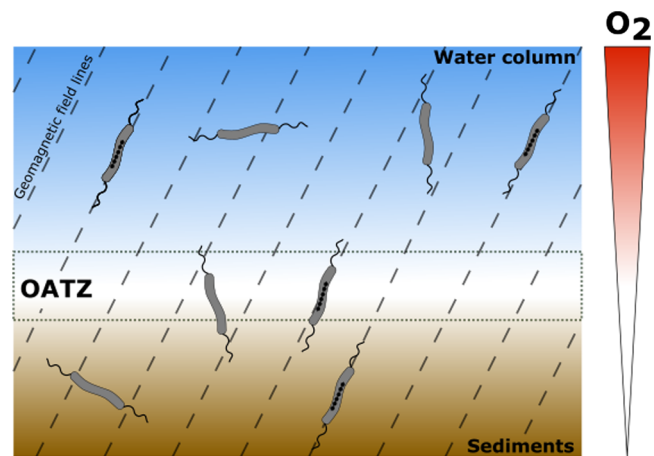


FIG. 9. Magnetotaxis in the oxico-anoxic transition zone (OATZ). The gray bacteria containing a magnetosome chain correspond to magnetotactic bacteria swimming along Earth's magnetic field lines, while the gray bacteria without a chain of magnetosome correspond to nonmagnetotactic bacteria that swim randomly From Fernández-Gubieda *et al.*, 2021.

adaptation of MTBs' behavior as the result of active sensing of a magnetic field, and hence magnetotaxis is widely considered to be purely passive. In the literature, magnetotaxis is always associated with another taxis: aerotaxis, which describes MTBs' ability to swim toward a preferred oxygen concentration and is most often referred to as magneto-aerotaxis.

A. Single cell magneto-aerotaxis

Aerotaxis is a form of chemotaxis for oxygen, and most of our current understanding of chemotaxis stems mainly from the extensively studied, peritrichously flagellated *E. coli*. These bacteria adapt their swimming behavior to travel up a chemoattractant gradient (Hansen, Endres, and Wingreen, 2008). The bacteria alternate between periods of run and tumble, and the swimming pattern is determined by the direction of the flagellar motor rotation. When the motor rotates in the CCW direction (as viewed from the flagella), several flagella form a loose bundle pushing the cell forward. This swimming pattern is called a run. When the motor reverses its rotation to CW, the bundle falls apart and the cell tumbles. During a tumble, the cell body is no longer propelled and diffuses, changing the orientation of the cell and its direction of motion; for further information, see Sec. II.B.1. Monopolar flagellated bacteria, such as marine vibrio, move forward through CCW rotation (run) of the flagella and move backward through CW rotation (reversal) (Stocker, 2011). Cells adapt their swimming behavior as they swim up the chemoattractant gradient by increasing the durations of their runs and by either increasing or decreasing their swimming speed. *E. coli*, for instance, has been shown to perform chemokinesis, i.e., increase its speed up the chemoattractant gradient, whereas others such as *Burkholderia contaminans* have exhibited the opposite behavior (Uday Bhaskar *et al.*, 2015; Bouvard *et al.*, 2022).

MTB aerotaxis differs from chemotaxis because MTBs travel both up and down the oxygen gradient, depending on whether they are in the oxic or the anoxic zone, toward their preferred oxygen concentration. Tracking of *Magnetospirillum gryphiswaldense* MSR-1 MTBs showed that MTBs regulate their speed and swimming behavior based upon the oxygen content in their local environment (Lefèvre *et al.*, 2014; Vincenti, 2019). MTB swimming speed distributions at low oxygen concentrations are bimodal with two maxima located at around 20 and 40 $\mu\text{m s}^{-1}$. At higher oxygen concentrations, the second maxima disappears and the distributions become monomodal, with longer tails at higher speeds (Vincenti, 2019).

B. Collective magneto-aerotactic motion

As MTBs migrate toward their preferred habitat, a region of high bacterial density forms in the region with the ideal oxygen concentration, known as the band (Guell *et al.*, 1988). The formation of bands is not limited to MTBs and occurs for many types of bacteria that live in gradient environments (Fischer and Cypionka, 2006; Stricker *et al.*, 2020). Aerotactic bands are recreated outside MTBs' natural habitat by performing capillary assays (Lefèvre *et al.*, 2014). A MTB suspension is used to fill a glass microcapillary that is then sealed on one

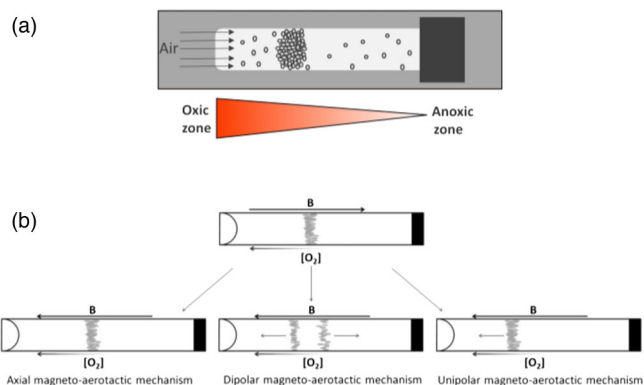


FIG. 10. (a) Band formation in a capillary assay where one end is sealed (the anoxic end) and the other end is open, allowing for oxygen diffusion (the oxic end). (b) Different types of magneto-aerotactic behavior. From Lefèvre *et al.*, 2014.

end (which will become the anoxic side) while the other end remains open (the oxic side), allowing oxygen to be exchanged between the bacterial suspension and the surrounding air. An oxygen gradient builds up progressively through diffusion of oxygen inside of the capillary and by consumption of oxygen by the bacteria (Fig. 10). In the Northern Hemisphere, the oxygen gradient and Earth's magnetic field lines are antiparallel. Hence, for a homogeneous field pointing toward the anoxic end of the capillary, a band forms inside the capillary where the preferred oxygen concentration of the bacteria is. Studies showed that, depending on the MTB species, the magnetic field or the oxygen gradient is used by the MTBs as a guide toward the ideal oxygen concentration, leading to three different types of magneto-aerotaxis: polar magneto-aerotaxis, axial magneto-aerotaxis, and unipolar magneto-aerotaxis (Lefèvre *et al.*, 2014).

A reversal of the magnetic field once the band has formed and does not move is used to decipher the magneto-aerotactic behavior. If the magnetic field is used by the bacteria only as an axis of motion and does not further influence the bacteria's swimming behavior by associating an additional directional axis, magneto-aerotactic behavior known as axial magneto-aerotaxis occurs. Axial magneto-aerotaxis has been observed in MSR-1 and AMB-1, the two most studied species. In the case of polar magneto-aerotaxis, in which the field is reversed and points toward the oxic side of the capillary, the bacteria in the band swim away from the band in both the oxic and anoxic directions. In this case, as described using the one-dimensional model shown in Eqs. (24)–(26), the reversal rate of the bacteria increases when the oxygen concentration is greater than the ideal oxygen concentration for MTBs and bacterial swimming is antiparallel to the magnetic field or when the oxygen concentration is below the MTBs' preferred oxygen concentration and the swimming is parallel to the magnetic field. This shows that the oxygen gradient does not direct the polarity of bacterial swimming but that the magnetic field does. In this instance, bacteria use the magnetic field direction as a proxy for the oxygen gradient, as is the case with SS-5 bacteria. In unipolar magneto-aerotaxis, the bacteria swim away from the band in only one direction upon field reversal. Some bacterial species have been found to show a

mix of polar and axial magneto-aerotaxis, perhaps as a form of bet-hedging strategy.

As described, magneto-aerotaxis differs from chemotaxis because MTBs travel both up and down the oxygen gradient in search of the ideal oxygen concentration. Chemotaxis was mathematically described by Keller and Segel (1971) as

$$u_t = \nabla[k_1(u, v)\nabla u - k_2(u, v)u\nabla v] + k_3(u, v), \quad (22)$$

$$v_t = D_v\Delta v + k_4(u, v) - k_5(u, v)v, \quad (23)$$

where u corresponds to the cell density, v is the concentration of the chemoattractant, k_1 corresponds to the diffusivity of the cells, k_2 is the chemotactic sensitivity of the cells, k_3 is the cell growth and death rate, and k_4 and k_5 are the production and degradation rates of the chemoattractant, respectively.

A one-dimensional model for magneto-aerotaxis was elaborated as (Lefèvre *et al.*, 2014)

$$\delta_t\rho_L = v\delta_x\rho_L - k_{LR}\rho_L + k_{RL}\rho_R, \quad (24)$$

$$\delta_t\rho_R = v\delta_x\rho_R - k_{RL}\rho_R + k_{LR}\rho_L, \quad (25)$$

$$\delta_t c = D\delta_x^2 c - k(c)(\rho_L + \rho_R), \quad (26)$$

where ρ_L and ρ_R correspond to the number of bacteria moving to the right and to the left of the band, respectively, k_{LR} and k_{RL} are the rates at which bacteria perform reversals from right to left and left to right, respectively, D is the diffusion of oxygen in water, and $k(c)$ is the bacterial concentration-dependent consumption rate of the oxygen. One can determine k_{LR} and k_{RL} using either basal switching rates or increased switching rates. The increased switching rate is used under oxic conditions (the oxygen concentration considered is greater than the preferred oxygen concentration) if the swimming direction of the bacteria is up the oxygen gradient for the case of axial magneto-aerotactic bacteria or antiparallel to the magnetic field direction for dipolar magneto-aerotactic bacteria. Under anoxic conditions (when the oxygen concentration is smaller than the preferred oxygen concentration), the increased switching rate is applied if the swimming direction of the bacteria is down the gradient in the case of axial sensing bacteria or parallel to the magnetic field direction for dipolar magneto-aerotactic bacteria. For unipolar magneto-aerotactic bacteria, k_{LR} and k_{RL} depend on the oxygen gradient in one regime and on the direction of the magnetic field in the other. Another model, describing chemotaxis in the presence of an external field (such as gravity and magnetic fields), was used to characterize the stochastic strategies for directional swimming of MTBs and to study the competition between the magnetic alignment of the cells to Earth's magnetic field lines and the active reorientation of the cells (Codutti *et al.*, 2019). This model shows that chemotactic efficiency is highest when the magnetic field is parallel to the oxygen gradient. However, magnetic orientation provides MTBs with an advantage and improves chemotaxis even when the angle between the magnetic field lines and the oxygen gradient is large.

These models fail to fully explain the complexity of the MTB swimming behavior, which has been observed experimentally. For instance, they do not fully explain and do not take into account the different measured swimming speeds of bacteria at varying oxygen concentrations and the swimming speeds that differ depending on whether they are swimming toward the band from the oxic or the anoxic side of the band. The one-dimensional model also assumes an aerotactic efficiency for band formation that is proportional to the cosine of the angle difference between the direction of the oxygen gradient and that of the magnetic field (Bennet *et al.*, 2014). However, experimental results have shown that aerotactic band formation is not altered when the magnetic field is tilted up 45° compared to the oxygen gradient direction, and bands still form when the magnetic field is orthogonal to the oxygen gradient (Bennet *et al.*, 2014). For MTBs, aerotaxis dominates over alignment to a magnetic field. For weak fields, the alignment of the cells with the magnetic field lines is not strong enough to perfectly constrain the cell body or to prevent the cells from exploring their environment and finding the ideal oxygen concentration to form a band. The rate at which the bands form in this instance will be slower than when the magnetic field is antiparallel to the oxygen gradient. These results show that the full complexity of MTB swimming behavior in gradient environments has yet to be fully understood and can be described only by a three-dimensional model taking into account the fluctuations of the MTB swimming behavior according to direct changes in sensing of their local physicochemical environment.

C. Control of the oxygen gradient

Studies of bacteria outside of their natural habitat have traditionally taken place in static oxygen concentrations of 21% or in uncontrolled gradients inside microcapillaries; see Sec. IV.B. Recent developments in microfluidic technologies allow for the spatial and temporal control of cells and their environment at the micrometer scale, permitting researchers to study cells under conditions closer to those of their natural habitat. Controlled gradients inside microfluidic devices have been generated through the controlled diffusion of laminar flows (Grant *et al.*, 2022), diffusion between a source and sink of different concentrations (Sip, Bhattacharjee, and Folch, 2011), and use of spatially confined chemical reactions (Chen, King *et al.*, 2011).

Controlled diffusion of laminar flows is the most well-established method for oxygen gradient control in micro-devices. In this instance, a polydimethylsiloxane (PDMS) membrane separates the channel of interest containing cells from the control channels containing gas. PDMS is gas permeable and allows the rapid diffusion of gases into the channel containing the cell suspension. The source fluid in the control channel rapidly diffuses to control the dissolved gas environment experienced by the cells. Spatial oxygen gradients ranging from 0% to 100% were established by Lo, Sinkala, and Eddington (2010) in the response of cells to reactive oxygen species. Oxygen concentrations can also be modulated by in-device reactions, which either consume or release oxygen. This technique eliminates the need for pressurized gas tanks but requires a careful balancing of reaction to kinetics to obtain the desired gas pressures.

Chen, King *et al.* (2011) developed a device consisting of a pair of reactions, one scavenging and the other releasing oxygen, which occur in two separate channels, each of which flanks the central channel containing a cell culture. A stable and linear gradient is produced across the cell culture channel. The previously described gradients were all characterized using a fluorescent ruthenium complex that has a decreasing fluorescence intensity for an increasing oxygen concentration following the Stern-Volmer equation,

$$\frac{I_0}{I} = 1 + K_q \tau_0 [\text{O}_2], \quad (27)$$

where I_0 and τ_0 are the intensity of fluorescence and excited state lifetimes, respectively, in the total absence of oxygen, $[\text{O}_2]$ is the oxygen concentration, and K_q is the quenching constant.

The full extent of opportunities these microfluidic options offer has yet to be applied to studies focusing on MTBs. To date MTBs have been tracked only in microfluidic channels containing different oxygen concentrations, thanks to the stream of laminar flows of two different gases [either one with a mixture of 80% oxygen and 20% nitrogen and the other with nitrogen (Vincenti, 2019) or one with air and the other with N_2 (Li *et al.*, 2011)] in two channels parallel to the one containing the cell suspension. Using a device similar to that shown in Fig. 11, the oxygen content obtained in the central channel containing the MTBs ranged from 0% to 20% (Vincenti, 2019).

V. COLLECTIVE MOTION

Bacteria (Aranson, 2022) as well as magnetic particles (Snezhko, 2016) display a myriad of collective motion of different natures. By combining the features of both bacterial and magnetic matter, MTB suspensions exhibit unique self-assembled structures and hydrodynamic instabilities. In this section, we review the magnetically controlled collective effects of those suspensions.

A. Actuation by magnetic fields

1. Bend and splay instabilities

Suspensions of microswimmers undergo aligning interactions known as nematic, which is described using the

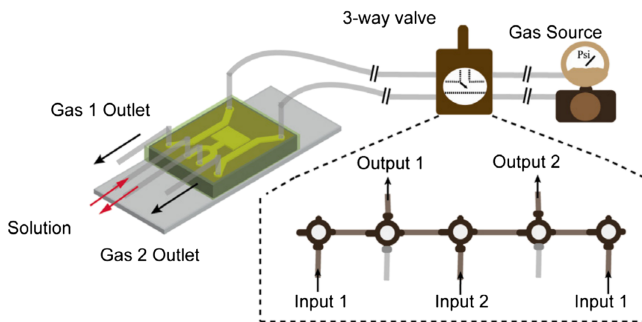


FIG. 11. Diagram of the microfluidic setup allowing the dynamic change of the oxygen gradient inside the chamber containing the cells. From Li *et al.*, 2011.

nematic tensor $\mathbf{Q} = \hat{\mathbf{n}} \hat{\mathbf{n}} - \mathbf{I}/3$. Nematic interactions can induce instabilities, depending on the concentration of microswimmers and their swimming behavior. At low concentrations, the homogeneous and isotropic state for both pushers and pullers can be destabilized above a critical level of activity, leading to large-scale density fluctuations for pushers and orientational fluctuations at every scale for pullers (Baskaran and Marchetti, 2009). For pushers (pullers), bend (splay) fluctuations, where only the parallel (orthogonal) component of the wave vector contributes, dominate (Wang *et al.*, 2018).

Magnetic microswimmers' direction of motion, and consequently nematic interactions, are controlled by magnetic fields. Koessel and Jabbari-Farouji (2019, 2020) showed how hydrodynamic instabilities were driven by a constant magnetic field in semidiluted suspensions of spherical magnetic microswimmers. Typical patterns of those instabilities are shown in Fig. 12. For low levels of activity and low magnetic fields, the suspension cannot be destabilized. For moderate activity and magnetic fields, pushers exhibit density fluctuations in their polarization field, forming sheets perpendicular to the field that travel toward the field direction governed by bend fluctuations. These bend fluctuations induce shear flow layers between the sheets that are further amplified by the unbalanced magnetic and hydrodynamic torques. In addition, the density of microswimmers increases in the zones where the divergence of the polarization field is negative. For the same activity and magnetic field, pullers exhibit alternating “pillarlike” flows antiparallel to the field that are governed by splay fluctuations. While increasing the field, the magnetic torque prevents instability formation, and the homogeneous polar state becomes stable again. These instabilities offer the possibility of distinguishing pusher microswimmers from pullers.

2. Self-assembly at surfaces

Active colloids and microswimmers undergo phase separation and 2D crystallization at surfaces. While phase separation of active colloids has been attributed mostly to spatial

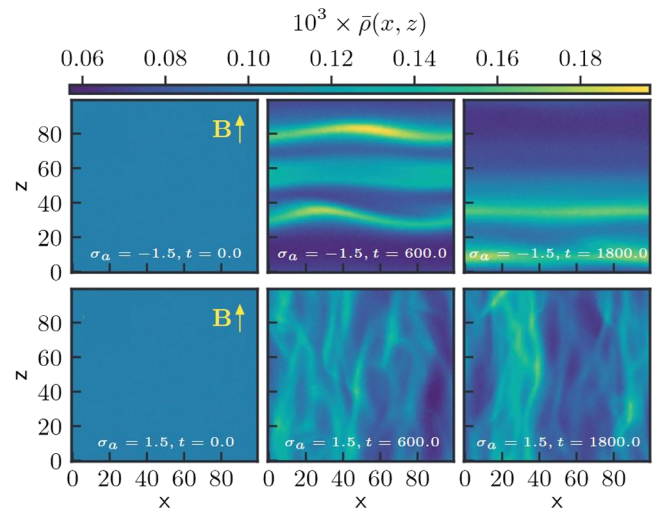


FIG. 12. Density projections averaged along the y axis from 3D nonlinear simulations at different time steps for pusher (top row) and puller swimmers (bottom row) in the unstable regime. From Koessel and Jabbari-Farouji, 2019.

variations of speed (Cates and Tailleur, 2015), hydrodynamics effects play an important role in the dynamics of active self-assembly at surfaces (Singh and Adhikari, 2016). From an hydrodynamic perspective, a microswimmer brought close to a surface generates a flow that in turn generates attractive forces and torques. Neighboring microswimmers are attracted to the central one at the surface, generating the self-assembly of crystalline clusters. Such clusters have been observed with the bacteria *Thiovulum majus* in the form of 2D hexagonal lattices (Petroff, Wu, and Libchaber, 2015; Petroff and Libchaber, 2018). The ability of *Thiovulum majus* to form 2D active crystals, despite the fact that it has never been observed in more widely studied bacterial strains such as *E. coli*, has been attributed to their large size (8 times that of *E. coli*), rapid swimming speed, and motility pattern, which is smoother than the run and tumble. Theoretical studies suggest that neither self-propulsion nor self-rotation is essential to generate self-assembly. The presence of the long-range flows produced by the microswimmers should theoretically be sufficient (Thutupalli *et al.*, 2018). In addition, the self-assembled crystals rotate due to rotlet dipole and quadrupole terms in the multiple expansion of the Stokeslet, which stem from the chirality of the microswimmers; see Sec. II.A.2 for further details (Singh and Adhikari, 2016).

Some of the aforementioned theoretical results and other aspects of collective motion of MTBs have been explored and demonstrated experimentally. These experimental results are discussed later. By applying a constant magnetic field pointed toward a surface, similar self-assembly has been observed with MTBs. Using the MTB AMB-1, Pierce *et al.* (2018) and Pierce, Wijesinghe, and Osborne (2020) were the first to characterize the behavior of magnetically controlled clusters. To establish the emergence of an ordered state, they measured the computable information density $CID \equiv L(x)/L_0$, where

$L(x)$ is the file size of the compressed microscopy images by a lossless compression algorithm and L_0 is the original file size. This quantity is related to the Shannon entropy, which quantifies the lack of information in a system and can be assimilated to a measure of order by analogy with the Boltzmann entropy for a system at equilibrium (Martiniani, Chaikin, and Levine, 2019). Note that the CID provides insight on the hidden order and the drops of entropy of an out-of-equilibrium system without specifying the order parameter. The influence of the magnetic field amplitude on the drops of the CID is shown in Fig. 13. Tuning the magnetic field strength influences the kinetics of the hidden order. For a moderate field of 1 mT (10 Oe), the order reaches a stable state in a few seconds, while for a strong field of 10 mT (100 Oe) the order increases with decreasing speed over time. A similar study using multicellular MTBs showed an analogy with a phase transition between an active gaseous state and an active fluid state by increasing the field strength, which tends to increase the cluster density and decrease the effective temperature of the cells (Petroff *et al.*, 2022). Moreover, by measuring the radial distribution function $g(r) = 4\pi r^2 \rho dr$ and the structure factor $S(q) = \rho(q)\rho(-q)/N$, where $\rho(q)$ is the Fourier transform of the density and N is the number cells, one can see that the system behaves like a compressible fluid because of the sharp peak of $S(q)$ at $q = 0$. By increasing the magnetic field from 0.9 to 4 mT, the density of clusters increases, leading to porous connected clusters, which is reminiscent of a percolation transition (Sanoria, Chelakkot, and Nandi, 2022). Control of the motion of the self-assembled clusters is achieved by adding an in-plane magnetic field to the magnetic field pointed toward the surface. Surprisingly a supplementary in-plane field smaller than 0.5 mT translates the clusters in the orthogonal direction with respect to the in-plane component, with a speed proportional to the

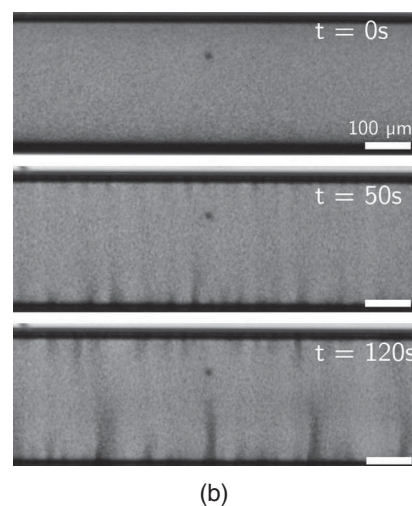
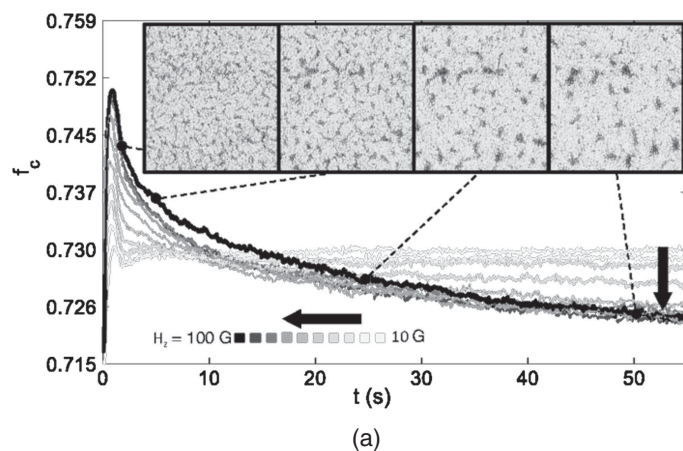


FIG. 13. (a) Self-assembled clusters of MTBs viewed from the top. The computable information density for a population was subjected to 10–100 G (1–10 mT) fields for 55 s toward the surface. As the field is decreased, the extent of the decay reduces until it remains nearly static in time for low values. Inset: selected microscopy images from the self-organization process associated with the red curve. (b) Self-assembled clusters of MTBs viewed from the side, where the magnetic field points toward the bottom surface. A uniform distribution of bacteria accumulates near the wall, and the concentration instability emerges. At longer times, plumes grow and cluster until a steady flow is obtained at $t = 2$ min. From Pierce *et al.*, 2018, and Théry *et al.*, 2020.

field-surface angle for small angles (Bente *et al.*, 2017). Increasing the in-plane field strength tends to translate the clusters in the direction of the field and destroys them beyond a critical value (Pierce, Wijesinghe, and Osborne, 2020).

While the self-assembly of MTBs is triggered by attractive flows near the surface, the accumulation of MTBs leads to a convective recirculating flow due to mass conservation (Pierce, Wijesinghe, and Osborne, 2020; Théry *et al.*, 2020). Therefore, bacteria close to the surface are attracted while those farther away are repelled by the convective flow. This bioconvection dynamic as well as the clusters' growth in the orthogonal direction to the surface were studied by Théry *et al.* (2020). In the orthogonal direction, the self-assembled clusters form plumes with a typical size and spacing set by the confinement height, reminiscent of the Rayleigh-Bénard hydrodynamic instability [Fig. 13(b)].

3. Self-assembly under a rotating magnetic field

Magnetic colloids submitted to rotating magnetic fields have been theoretically predicted (Gotze and Gompper, 2010) and experimentally demonstrated (Snezhko, 2016; Massana-Cid *et al.*, 2021) to undergo out-of-equilibrium self-assembly and pattern formation, which converts spinning motion into translation thanks to the interfaces being close together. Fusion and fission scenarios of clusters made of magnetic microswimmers in rotating fields were theoretically investigated and showed that linear chains of magnetic pullers were stable, while a pusher chain showed a succession of fission as the self-propulsion velocity increased (Guzmán-Lastra, Kaiser, and Löwen, 2016). Magnetoactive Janus colloids (Jaeger, Stark, and Klapp, 2013) were theoretically predicted to form hexagonal rotating crystals. This has been also been experimentally observed for synthetic magnetic microswimmers (Vach *et al.*, 2017), as shown in Fig. 14(a). The formation of these rotating crystals is driven by the hydrodynamic interactions between the rotating components, which induce a shear force $F \sim \eta\omega a^2 \ln(H/a)$, where ω is the angular velocity, a is the particle size, and H is the distance to the particle (Belovs, Bricis, and Cēbers, 2019). For the particles in the core of the crystal no motion occurs, because of the symmetric torque balance; only the particles at the border experience an unbalanced torque, leading to the rotation of the crystal (Yan, Bae, and Granick, 2015).

Regarding MTBs, different collective behaviors in rotating fields have been theoretically predicted. Belovs, Livanovičs,

and Cēbers (2017) predicted the possibility of obtaining synchronized circular motion of swarms with a diffusion coefficient directly linked to the field frequency,

$$D_{\text{eff}} = \frac{v_b^2}{6D_r[1 + (\omega/2D_r)^2]}. \quad (28)$$

MTB trajectories inside the swarms follow a hexagonal path that depends upon the number of cells. The angular velocity of the swarm also depends upon the number of MTBs and decreases when the cell density increases. Moreover, at high frequencies magnetic pullers form pairs of bacteria that synchronize and swim as a doublet (Belovs, Livanovičs, and Cēbers, 2019). Surprisingly some of the adopted trajectories are straight lines, with cells swimming straight ahead even when they are submitted to a rotating field. Periodic fourfold trajectories are also adopted.

Inspired by the Vicsek model describing flocking active matter, Liebchen and Levis (2017) developed the chiral-active-particle (CAP) model, which describes the collective behavior of rotating active particles such as MTBs in rotating fields. The CAP theoretical model shows one of two types of patterns, depending on the ratio between the rotation frequency and the interaction strength between the particles. When the ratio between aligning interactions and the rotation frequency is high, the particles can be phase locked parallel to each other and can form a macrodroplet. In the opposite situation, rotation limits the particles' interactions and leads to microflocks of different phases, as shown in Figs. 14(b) and 14(c).

B. Actuation by flow and a magnetic field

The collective motion of MTBs can also be triggered using counter-Poiseuille flow in addition to a magnetic field. Theoretical studies on microswimmers in counter-Poiseuille flow (Jibuti *et al.*, 2014; Lauga and Nadal, 2016), inspired by experiments with phototactic algae (Garcia, Rifaï, and Peyla, 2013), showed that only pullers lead to pearling instabilities, while pushers always remain stable. Surprisingly such clustering effects were observed in the MTB MC-1, despite it being considered a pusher, while it was oriented by a strong magnetic field in the opposite direction of the flow (Waisbord *et al.*, 2016a). This clustering instability was further studied theoretically by Meng, Matsunaga, and Golestanian (2018),

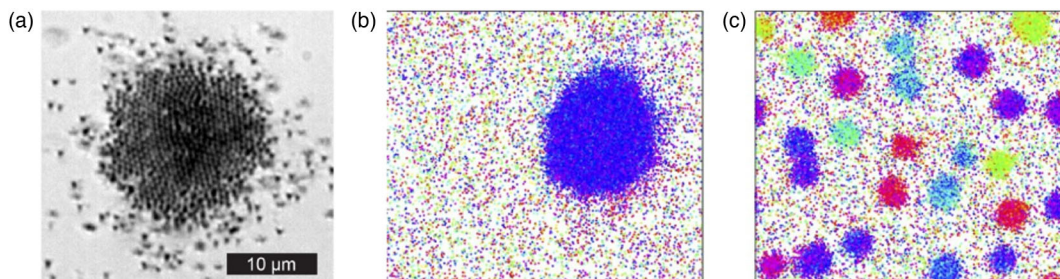


FIG. 14. (a) Image of a rotating crystal made of synthetic magnetic microswimmers. Particles with polar alignment and a single angular frequency can self-organize into (b) rotating macrodroplets and (c) microflock patterns. Differences in color indicate different orientations. From Liebchen and Levis, 2017, and Vach *et al.*, 2017.

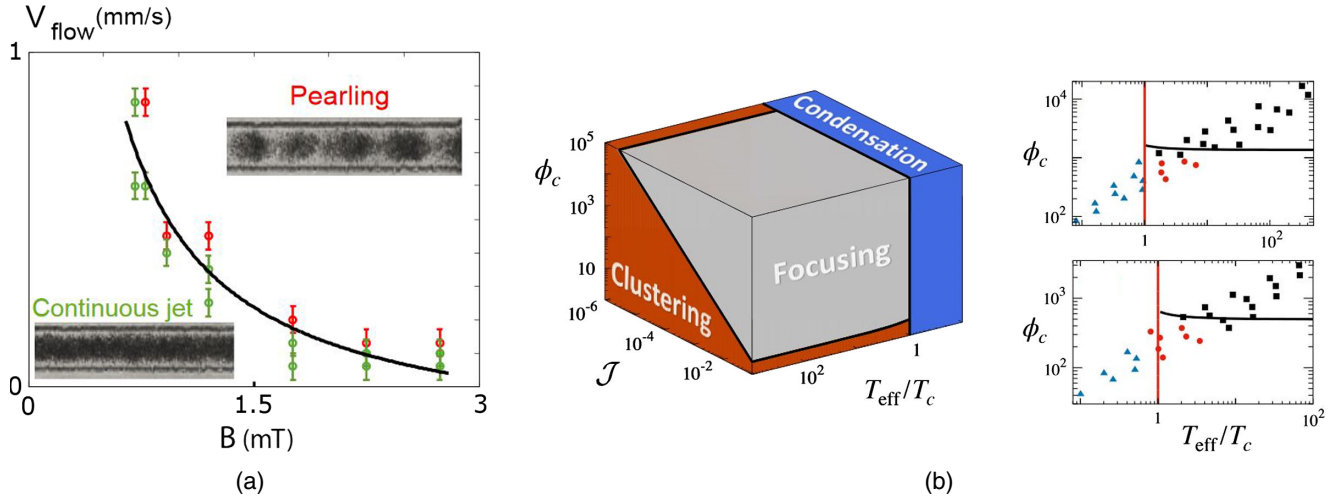


FIG. 15. (a) Phase diagram of the instability for various values of V_f and B . The red (dark gray) dots are the unstable jets, whereas the green (light gray) dots are the stable jets. The black line is the best adjustment with $V_f = a/B + c$, with $a = 0.630 \text{ mm mT s}^{-1}$ and $c = 0.19 \text{ mm s}^{-1}$. Adapted from [Waisbord *et al.*, 2016a](#). (b) Theoretical phase diagram in the $(T_{\text{eff}}/T_c, J, \phi_c)$ parameter space showing the focusing (triangles), pearling (dots), and condensation (squares). From [Meng *et al.*, 2021](#).

who showed that the state of the system was driven by the dimensionless number

$$\mathcal{B} = \frac{\mu_0 \rho_0 m^2 m B_{\text{ext}} v_f}{4 k_B T k_B T v_0}, \quad (29)$$

where μ_0 is the magnetic permeability, ρ_0 is the bacterial density, and v_f is the flow velocity. For $\mathcal{B} < 1$, a stable focused state is obtained with a Gaussian radial distribution identical to the single cell case; see Sec. III.B.1. This state can then be destabilized using a stronger field or stronger flow to obtain $\mathcal{B} > 1$. In this regime, a clustering state is obtained with a noncontinuous concentration profile along the channel's main axis [Fig. 15(a)]. The clusters travel along the channel at a speed set by $v_f - v_0$, which can lead to upstream swimming. Even if the MTB *Magnetococcus marinus* MC-1 is a pusher, the interaction with the magnetic field allows the Gaussian jet to be unstable above a critical magnetic stress. Note that the hydrodynamic interactions between the bacteria do not seem to play a major role in the instability, which is driven mainly by magnetism thanks to a high cell density ($\sim 32\%$ of the volume fraction) ([Waisbord *et al.*, 2016a](#); [Meng, Matsunaga, and Golestanian, 2018](#)).

For higher values of \mathcal{B} , a Bose-Einstein-like condensation has been predicted ([Meng *et al.*, 2021](#)) that is similar to that predicted for scalar active matter with diffusivity edges ([Golestanian, 2019](#)). This regime is characterized by strong confinement of the swimmers in the center of the channel, which can be considered the ground state by analogy with a Bose-Einstein condensate. This effect should be observed using swimmers that carry a large magnetic moment or using highly concentrated suspensions of magnetic microswimmers. The transition to the condensate state is described using a critical value of the effective temperature experienced by the microswimmers,

$$k_B T_{\text{eff}} = k_B T \left[1 + \frac{v_0^2}{DD_r} \left(\frac{k_B T}{m B_{\text{ext}}} \right)^2 \right]. \quad (30)$$

When the effective temperature of the system reaches the critical value $T_{\text{eff}} = T_c$, all the microswimmers reach the ground state, which is defined as the channel center, as a Bose-Einstein-like condensate would do. To construct the full phase diagram, the following two other quantities should be considered:

$$\mathcal{J} = \frac{m B_{\text{ext}} DD_r}{k_B T v_f v_0}, \quad (31)$$

which quantifies the ratio between the magnetic and thermal energy as well as the strength of propulsion and shear velocities versus diffusion, and

$$\phi_c = \frac{k_B T_{\text{eff}}}{\mu_0 \rho_0 m^2}, \quad (32)$$

which quantifies the role of the density-dependent effective diffusion of the system. The phase diagram of the system is shown in Fig. 15(b).

VI. RHEOLOGY

The active and magnetic aspects of MTBs can both induce rheological effects. Magnetorheological fluids (MRFs), which are made of solid magnetic particles dispersed into a liquid matrix, are already used in industry and in fundamental research to study phenomena like the glass transition ([Morillas and de Vicente, 2020](#)). Bacterial rheology is a growing field in which noteworthy effects have been observed and predicted ([Liu, Zhang, and Cheng, 2019](#); [Jana *et al.*, 2020](#); [Chui *et al.*, 2021](#)). MTB suspensions take advantage of these two characteristics to show features at the border of MRFs and active matter.

A. Magnetorheology

1. Magnetic stress and effective viscosity

In a suspension of passive magnetic particles, the torque induced by the magnetic field gives rise to a magnetic

stress contribution that vanishes for particles that are perfectly aligned with the field, as given by (Ilg, Kroger, and Hess, 2002)

$$\sigma_m = \frac{1}{2}\rho_0 m B_{\text{ext}} (\hat{\mathbf{B}}\mathbf{e} - \mathbf{e}\hat{\mathbf{B}}), \quad (33)$$

where $\vec{B}_{\text{ext}} = B_{\text{ext}} \hat{\mathbf{B}}$. The time response of the particle alignment depends on both the Brownian relaxation time $\tau_B = 3\eta V_h/k_B T$, where V_h is the hydrodynamic volume, and the Néel relaxation time $\tau_N = \tau_0 e^{K V_c/k_B T}$, where K is the effective anisotropy constant and V_c is the magnetic core volume (Büscher *et al.*, 2004). When the magnetic field is switched off the particles relax, with the effective relaxation time given by $\tau_{\text{eff}}^{-1} = \tau_B^{-1} + \tau_N^{-1}$. When magnetic particles rotate due to a magnetic torque, an additional flow arises that influences the local fluid vorticity. The competition between the flow-induced and the magnetic-torque-induced alignment of the particles gives rise to the so-called magnetoviscous effect. While small particles relax through the Néel process, particles above a critical volume follow a Brownian relaxation due to the exponential dependency of the Néel time with respect to the particle's volume. Thus, only large enough particles considered "magnetically hard" will contribute to this effect (Odenbach and Thurm, 2002). For magnetite, this critical diameter is 30 nm, with the knowledge that magnetosome crystals range in diameter from 30 to 120 nm (Klumpp *et al.*, 2019).

In a constant magnetic field, particle rotation in a flow is hindered, which leads to an increase of the effective viscosity (McTague, 1969). This effective viscosity is given as

$$\Delta\eta = \frac{2}{3}\phi\eta \frac{\gamma B_{\text{ext}} - \tanh(\gamma B_{\text{ext}})}{\gamma B_{\text{ext}} + \tanh(\gamma B_{\text{ext}})} \sin^2(\theta_{B/\Omega}), \quad (34)$$

where ϕ is the volume fraction of the particles, γ is the shear rate, and $\theta_{B/\Omega}$ is the angle between the magnetic field and the flow vorticity. This additional viscosity is greater if the magnetic field is pointed parallel to the flow direction. Particles with a larger aspect ratio give rise to a larger contribution in the viscosity since such elongated particles induce larger resistance in a flow field (Aoshima *et al.*, 2002).

In an alternating magnetic field, the effective viscosity is given by (Bacri *et al.*, 1995)

$$\Delta\eta = \frac{2}{3}\phi\eta \frac{\Omega - \omega_p}{\Omega}, \quad (35)$$

where Ω is the vorticity and ω_p is the particle angular velocity. In such external fields particles rotate without any preferable direction of rotation, and on average $\omega_p = 0$. Any flow for which $\Omega \neq 0$ can break the symmetry and promote a sense of rotation. If $\Omega > \omega_p$, the additional viscosity is positive, as in the case of a constant field. If $\Omega < \omega_p$, particles spin up the flow and inject kinetic energy into the fluid, resulting in a decrease in viscosity called the negative viscosity effect (Bacri *et al.*, 1995).

2. Odd viscosity in chiral fluids

Active fluid corresponds to matter that is made of constituents that are powered and set into motion by external or

internal energy sources. The physical properties of these fluids show significant deviations from those in standard equilibrium thermodynamics. To understand how these fluids flow, one needs to study how the active particles interact with the surrounding fluid and uncover the equations that govern these interactions.

Chirality was first defined by Kelvin in 1893 as an object whose image in a plane mirror cannot be superimposed onto itself. Chirality, however, not only relates to the shape of an object but also is found in motion patterns and trajectories. Local injection of energy into a fluid forces its constituents into linear motion or forces them to rotate. Chiral active matter is hence described as a material whose constituents are self-spinning rotors that self-inject energy and angular momentum into the fluid at the microscale (Liebchen and Levis, 2022). Biological examples of chiral active matter include sperm cells (Riedel, Kruse, and Howard, 2005), circling bacteria at surfaces (Lauga *et al.*, 2006; Di Leonardo *et al.*, 2011), and MTBs in rotating fields. Bacterial suspensions of MTBs in rotating magnetic fields are, in other words, chiral self-propelled matter. As chiral active particles swim in a fluid, they locally actuate the fluid surrounding them, giving rise to hydrodynamic interactions between different chiral active particles and generating collective motion and phenomenology of the chiral active particles; see Sec. V.B.

Chiral active fluids, like any viscoelastic material, have a viscosity. In the case of Newtonian fluids, viscosity is a measure of a fluid's resistance to a velocity gradient and arises mathematically as a symmetric viscosity tensor η_s that is a coefficient of proportionality between viscous stress and the strain rate. When perturbed by external forces, i.e., when stress is applied to systems at equilibrium, the resulting strain rate of the system is proportional to the applied stress. The Onsager reciprocity relations stipulate that viscosity is symmetric because time-reversal symmetry holds for systems at equilibrium. As previously described, however, chiral active fluids are out-of-equilibrium systems that break time-reversal symmetry. What, then, is the viscosity of chiral active fluids? Banerjee *et al.* (2017) showed that the equations describing active chiral media gave rise to an asymmetric viscosity tensor with off-diagonal terms. Such terms give rise to the so-called odd (or Hall) viscosity. Odd viscosity does not create heat or entropy as dissipative viscosity does and physically characterizes the orthogonal stress response of the chiral active particles on the imposed flow.

B. Bacterial suspension rheology

Haines *et al.* (2008) calculated the effective viscosity of a two-dimensional suspension of self-propelled disks meant to mimic a bacterial suspension with a two-dimensional volume fraction ϕ ,

$$\eta_{\text{eff}} = \eta \left(1 + 2\phi + \frac{c}{2\pi\eta\epsilon_0} \frac{1 + 2\lambda(2 + \lambda)}{(1 + \lambda)^3} \phi \sin(2\alpha) \right), \quad (36)$$

where c is the force strength generated by the flow of the self-propelled particles, λ represents the distance between the center of the disk to the flagella, α corresponds to the orientation of the self-propelled disk, and ϵ_0 is a constant

equal to the amplitude of the strain rate of the flow. This work predicts that with an increase in the volume fraction of bacteria in a bacterial suspension the effective viscosity should decrease. A decrease in viscosity can be interpreted as a compensation of the energy lost by dissipation by injection of energy into the system by the transformation of the chemical energy available in the environment into fluid motion by the bacteria. The elaborated model shows that in certain cases the viscosity could even become negative. A negative viscosity would result from overcompensation of the energy being dissipated by the energy injected in the system by the flagellar rotation.

Active-particle rheology was experimentally studied using generated shear flows comparable to the ones generated by the active particles with low shear rates. Sokolov and Aranson (2016) imposed a vortex flow generated by a magnetic particle placed in a rotating magnetic field in a bacterial suspension of a pusher petrichous bacteria called *Bacillus subtilis*. Once the rotation of the particle ceases, the generated vortex flow decreases due to viscous friction. The timescale at which the decrease of the vortex flow occurs is proportional to the shear viscosity of the bacterial suspension. Gachelin *et al.* (2013) showed similar results when measuring the viscosity of an active suspension of *E. coli* bacteria as a function of the shear rate using a Y-shaped microfluidic channel. They showed that the viscosity of the bacterial suspension was lower than that of the surrounding fluid for shear rates down to 1 Hz. The shear rate range was expanded by López *et al.* (2015), who applied Couette flows with shear rates as low as 0.04 Hz (Fig. 16). Couette flows correspond to the flow of a fluid between two surfaces, one of which is moving tangentially relative to the second surface. For a fixed Couette flow shear rate, the bacterial suspension viscosity dropped to 0 for a wide range of cell concentrations, which is reminiscent of superfluid regimes. Superfluidity was measured experimentally in *E. coli* bacterial suspensions. Similar experiments were conducted with puller bacteria, but the lowest shear rate used was 4 Hz, which led to an increase of the viscosity of the bacterial

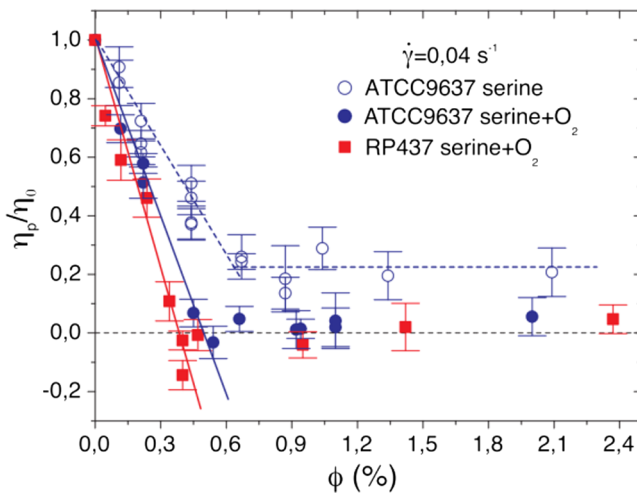


FIG. 16. Variation of the viscosity of an *E. coli* suspension as a function of the volume fraction of bacteria in oxygenated conditions (filled symbols) and deoxygenated conditions (empty symbols). From López *et al.*, 2015.

suspension. The tunability of the viscosity of bacterial suspensions opens up new avenues of research and promising applications in the microfluidics field.

C. Magnetoactive suspension rheology

1. Motor-brake effect

The application of a magnetic field to a MTB suspension aligns the bacteria with respect to the applied field. Aligned and oriented swimming of bacteria due to the magnetic field inside a bacterial suspension impacts the rheological properties of the suspension. The total stress of the system $\bar{\bar{\Sigma}}$ is characterized by the sum of both the fluid stress and the particle stress $\bar{\bar{\Sigma}}_p$ and is mathematically described by (Saintillan, 2010)

$$\bar{\bar{\Sigma}} = -P\bar{\bar{I}} + 2\eta_s\bar{\bar{E}} + \bar{\bar{\Sigma}}_p, \quad (37)$$

where P is the fluid bulk pressure, η_s is the suspending fluid dynamic viscosity, $\bar{\bar{I}}$ is the identity tensor, and $\bar{\bar{E}}$ is the strain-rate tensor.

Swimming by the bacteria generates work. The maximal work per unit volume is known as the energy density $n\sigma_0$. By dividing $\bar{\bar{\Sigma}}_p$ by the energy density, the particle stress can be

described as a dimensionless factor $\bar{\bar{\Sigma}}_p^{\sim}$. Bacterial swimming is given by the characteristic time t_h needed for the bacteria to move the fluid along a distance equal to its size due to the effect of its permanent force dipole, which is proportional to the rotational friction coefficient and inversely proportional to the energy density. This timescale is used to describe the persistent directionality of the bacterial swimming's trajectory and to characterize the activity number $A = 1/t_h D_R$, where D_R is the rotational diffusion time. Using A , the Péclet number Pe_H , and the magnetic Péclet number Pe_m , which corresponds to the ratio of the magnetic relaxation time with respect to the rotation diffusion of a bacteria, the (x, y) component of the active-particle stress for bacteria swimming in a direction \vec{e} can be mathematically described as (Saintillan, 2010; Vincenti, Douarache, and Clement, 2018)

$$\begin{aligned} (\bar{\bar{\Sigma}}_e)_{xy} = & \frac{1}{2} \langle e_x^2 e_y^2 \rangle \frac{Pe_H}{A} + \frac{3}{A} \langle e_x e_y \rangle \\ & + \frac{Pe_m}{A} \langle [e_x e_y b_y - b_x (1 - e_x^2)] e_y \rangle, \end{aligned} \quad (38)$$

where b_x and b_y are the x - and y -axis components of the magnetic field \vec{b} and $\epsilon = 1$ for puller particles, whereas $\epsilon = -1$ for pusher particles. The first and second terms of the particle stress equation correspond to passive contributions representing the drag on the surface of the particle due to shear flow and the diffusion of the cell, respectively. The third term relates to the swimming of the bacteria, and the last term represents the stress generated by the rotation of the bacteria driven by a magnetic field.

Three different regimes arise from the particle stress equation: one where the alignment by the flow is negligible

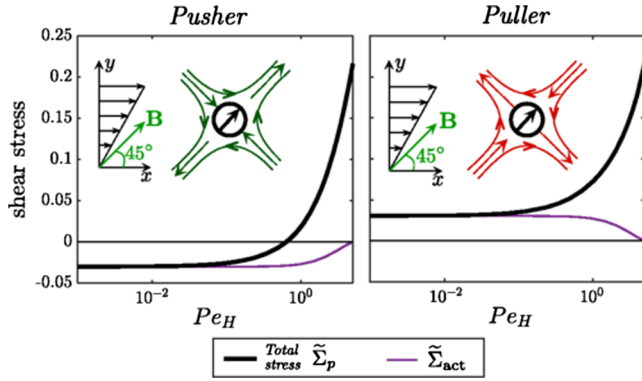


FIG. 17. Particle shear stress as a function of the hydrodynamic Péclet number for a fixed $Pe_M = 1$ fixed particle activity value $A = 10$. From [Vincenti, Douarache, and Clement, 2018](#).

compared to the alignment by the magnetic field ($Pe_m \gg Pe_H$), a second regime where the alignment is due to equal contributions by the flow and the applied magnetic field, and a third regime where the alignment of cells is mainly the result of the applied shear flow ($Pe_H \gg Pe_m$). When one considers the first regime, if $Pe_H \ll 1$ and for any Pe_m greater than Pe_H , the diffusion and magnetic components of the particle shear stress equation (38) compensate for each other and the particle stress is due only to drag stresses on the surface of the particle and the swimming activity of the particle. In the case where Pe_H is almost null, the particle stress, now called actuated stress, is due solely to the swimming activity of the particle, which is induced by the presence of a magnetic field. [Vincenti, Douarache, and Clement \(2018\)](#) showed that in these low Pe_H regimes both pusher and puller particle orientations are due to the presence of a magnetic field. Both pusher and puller swimmers are able to increase the shearing of the fluid (motor state) or decrease it (brake state) depending on the magnitude and direction of the magnetic field applied (Fig. 17). For a given Pe_m , the effect is maximal when the extensional and compression axis of the flow created by the particles are aligned with the magnetic field (motor state) or perpendicular to the field (brake state).

2. Magnetoactive pumping

The hydrodynamic response of MTBs under flow and in confined geometries is tuned by the application of a magnetic field. Depending on the applied field strength and orientation, the magnetic alignment of the cells under shear flow and the interaction and accumulation of bacteria at a surface are either hindered or accentuated. [Alonso-Matilla and Saintillan \(2018\)](#) theoretically described the behavior of two-dimensional confined MTBs in the presence and the absence of a magnetic field using a continuum kinetic model. According to their model, in the absence of a magnetic field, MTBs accumulate equally at the top and bottom boundaries with an average net polarization of the MTBs directed toward the boundaries. Applying a magnetic field in any direction that is not focused directly on the boundaries results in a torque acting on the MTBs competing with the natural polarization of the particles at the boundary surfaces (Fig. 18). This competition between the inherent polarization and the torque is transmitted to the

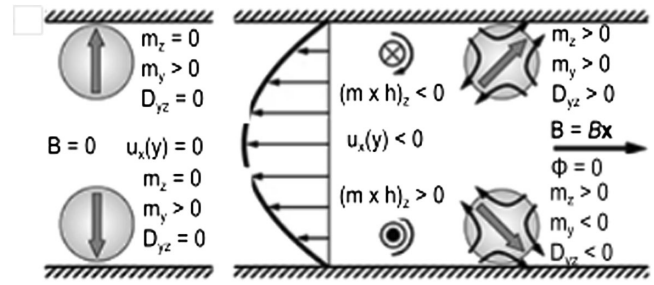


FIG. 18. Disturbance flow generation by a magnetic field. Left sketch: average particle distribution and orientation in the absence of a magnetic field. $B = B\mathbf{x}$ is a uniform magnetic field with a unit vector h , \vec{m} is the magnetic moment of the particle, Φ corresponds to the angle of the magnetic field, u is the fluid velocity, and D is the second orientational moment of the distribution function representing the nematic alignment of the cells. Right sketch: flow created by the combined effect of a magnetic field and active stresses on a suspension of pusher microswimmers. In the case of puller microswimmers, the magnetic stress remains the same, while the sign of the active disturbance flow changes. From [Alonso-Matilla and Saintillan, 2018](#).

fluid via viscous drag. The model of [Alonso-Matilla and Saintillan](#) predicted that the magnetic torque at the top and bottom surfaces of the confinement are opposing. The resulting magnetic shear stress is predicted to induce a flow. Their work highlights that the flow increases with increasing (weak to moderate) magnetic field strengths. However, if the magnetic field is too strong, the cell alignment with the field direction prevents the polarization of the cells at the confinement surfaces. Hence, no magnetic torque at the surfaces occurs and no flow is produced in the channel.

These theoretically predicted internally driven flows resemble the spontaneous flows that have been experimentally observed in confined suspensions of pusher *B. subtilis* bacteria or sperm cells ([Creppy et al., 2016](#); [Wioland, Lushi, and Goldstein, 2016](#)). However, the model described here suggests that the flow strength would be controlled and turned on and off at will by simply varying the magnetic field intensity and direction. These interesting theoretical results have yet to be experimentally proven.

VII. OUTLOOK

In this section, we propose potential directions for future studies, emphasizing the key role of MTBs in the research fields of biological microswimmers, active matter, and complex fluids.

A. Single cell motion

MTBs show a great diversity of flagellar apparatus, which raises questions regarding the potential connections among the flagellar motor architecture, the distribution of flagella, the hydrodynamics, the magnetism, and the motility patterns. Fluorescent labeling of the flagella is an efficient technique to distinguish the swimming behavior and the transitions among the puller, pusher, and wrapped states. Thus far this technique has been used with peritrichous (*E. coli*), lophotrichous

(*Pseudomonas putida*), and amphitrichous (AMB-1) bacteria and could be an efficient tool to study the bilophotrichous fast-swimming MTBs MO-1 and MC-1, which have a unique motor architecture and unique swimming behaviors with synchronized pushing-pulling flagellar bundles. However, genetic systems have yet to be developed for these species.

MTB motion guided by magnetic fields shows differences with the purely passive Langevin paramagnetic model. The variability of the magnetosome alignment with the cell body and the distribution of magnetic moments in a cell population play an important role. The molecular mechanism responsible for the nonthermal noise in the cells' orientations still needs to be unraveled.

B. Complex media

Bacterial motion in crowded environments differs from the motion in bulk media. MTBs in 2D arrays of obstacles are efficiently guided by a physiological magnetic field, even when submitted to an external counterflow, but their guided motion in 3D porous media is still elusive. Combining of the hops and traps model of motility in 3D porous media with a magnetotaxis model will be an interesting tool to describe their motion, knowing that these bacteria are found in sedimentary environments. Supplementary types of complex media such as fluids like liquid crystals or polymeric solutions, which have already been used with nonmagnetic bacteria, and complex magnetic media that induce body forces in addition to torques should be considered.

C. Magneto-aerotaxis

MTBs have been receiving growing interest in the biomedical community. Their ability to migrate toward regions depleted in oxygen, such as cancerous tumors, and their inherent magnetic properties make them potential candidates for magnetic hyperthermia and targeted drug deliveries. However, to adequately guide and fine-tune the cellular response of MTBs in complex gradient environments, it is important to understand and have a working three-dimensional model of magneto-aerotactic behavior. This has yet to be achieved. Furthermore, magnetotaxis has always been considered a passive alignment of the bacteria to magnetic field lines, yet there is a growing amount of evidence suggesting that magnetic fields could actively influence bacterial behavior through active magnetoreception. Proteins sensitive to magnetic fields have been uncovered, and some of these proteins have been genetically found in MTBs. However, the calculated response of the proteins found to date in magnetic fields is weak and cannot fully account for the observed cellular activity (Meister, 2016). Studies focusing on how these proteins could influence MTB behavior or how MTBs perceive signals from these proteins and their environment are still scarce, however.

D. Collective motion

Collective motion of bacteria has been widely studied through the prism of active turbulence. Nevertheless, the impact of magnetotaxis on this phenomenon has been

insufficiently discussed. Moreover, several theoretical predictions about magnetically driven collective motion have been made, without any experimental proof, such as bend and splay instabilities or Bose-Einstein-like condensation. New collective patterns involving magnetotaxis and aerotaxis should also be investigated. The main challenge experimentalists will face in trying to prove these models is that they often require high concentrations of bacteria. On the one hand, it is important to have active motile cells to observe any of these theoretically predicted phenomena, and at high cell concentrations the nutrients present in the media might be consumed rapidly, potentially leading to a motility decrease on a short timescale. On the other hand, in the theoretical framework high cell density leads to magnetic dipole-dipole interactions, as has been shown with Bose-Einstein-like condensation. However, most of the studied collective motion takes place in the semidilute regime, where hydrodynamics dominates over magnetic interactions.

E. Rheology

Magnetic as well as active particles play a crucial role in the rheological behavior of the fluid. To date no rheological experiments have been done with MTBs despite some newly predicted effects such as the “motor-brake” or “magnetoactive pumping” effects. Rheological experiments, however, are challenging as far as the necessity of high bacterial concentrations and the loss of activity due to the fast nutrient consumption in such conditions are concerned.

ACKNOWLEDGMENTS

We thank the current and former members of the CEA Cadarache and the Light Matter Institute, as well as the former members of the Max Planck Institute of Colloids and Interfaces, where this research started. The project leading to this Colloquium received funding from the French National Research Agency for collaborative research with C. Cottin-Bizonne and E. Clément (Project No. PRC ANR-20-CE30-0034) and for a French-German collaboration with S. Klumpp (Project No. PRCI ANR-20-CE92-0051). Funding was also provided by the Excellence Initiative of Aix-Marseille University—A*Midex, a French Investissement d'Avenir program (AAP International 2018—MaTher), for collaboration research with S. Klumpp and S. Sanchez, and by the ITMO Cancer of Aviesan within the framework of the 2021–2030 Cancer Control Strategy, on funds administered by Inserm, and by France 2030.

REFERENCES

- Acosta-Avalos, D., *et al.*, 2019, *Eur. Biophys. J.* **48**, 513.
- Alert, R., J. Casademunt, and J.-F. Joanny, 2022, *Annu. Rev. Condens. Matter Phys.* **13**, 143.
- Alonso-Matilla, R., B. Chakrabarti, and D. Saintillan, 2019, *Phys. Rev. Fluids* **4**, 043101.
- Alonso-Matilla, R., and D. Saintillan, 2018, *Europhys. Lett.* **121**, 24002.
- Alphandry, E., 2020, *Drug Discov. Today* **25**, 1444.
- Aoki, I., 1982, *Bull. Jpn. Soc. Sci. Fish.* **48**, 1081.

- Aoshima, M., A. Satoh, R. W. Chantrell, and G. N. Coverdale, 2002, *J. Colloid Interface Sci.* **253**, 455.
- Aranson, I., 2022, *Rep. Prog. Phys.* **85**, 076601.
- Bacri, J.-C., R. Perzynski, M. I. Shliomis, and G. I. Burde, 1995, *Phys. Rev. Lett.* **75**, 2128.
- Bahaj, A., P. James, and F. Moeschler, 1996, *IEEE Trans. Magn.* **32**, 5133.
- Balkwill, D. L., D. Maratea, and R. P. Blakemore, 1980, *J. Bacteriol.* **141**, 1399.
- Banerjee, D., A. Souslov, A. G. Abanov, and V. Vitelli, 2017, *Nat. Commun.* **8**, 1.
- Bárdfalvy, D., H. Nordanger, C. Nardini, A. Morozov, and J. Stenhammar, 2019, *Soft Matter* **15**, 7747.
- Baskaran, A., and M. C. Marchetti, 2009, *Proc. Natl. Acad. Sci. U.S.A.* **106**, 15567.
- Bazylinski, D. A., and D. Trubitsyn, 2019, in *Magnetic Nanoparticles in Biosensing and Medicine*, edited by N. J. Darton, A. Ionescu, and J. Llandro (Cambridge University Press, Cambridge, England), pp. 251–284.
- Belovs, M., M. Bricis, and A. Cēbers, 2019, *Phys. Rev. E* **99**, 042605.
- Belovs, M., R. Livanovičs, and A. Cēbers, 2017, *Phys. Rev. E* **96**, 042408.
- Belovs, M., R. Livanovičs, and A. Cēbers, 2019, *Soft Matter* **15**, 1627.
- Bennet, M., *et al.*, 2014, *PLoS One* **9**, e101150.
- Bente, K., G. Kitenbergs, D. Kriman, K. Erglis, M. Belovs, D. Faivre, and A. Cēbers, 2017, [arXiv:1707.02827](https://arxiv.org/abs/1707.02827).
- Bente, K., S. Mohammadinejad, M. A. Charsooghi, F. Bachmann, A. Codutti, C. T. Lefèvre, S. Klumpp, and D. Faivre, 2020, *eLife* **9**, e47551.
- Berg, H. C., 2008, *Curr. Biol.* **18**, R689.
- Bhattacharjee, T., and S. S. Datta, 2019a, *Nat. Commun.* **10**, 2075.
- Bhattacharjee, T., and S. S. Datta, 2019b, *Soft Matter* **15**, 9920.
- Bianchi, S., F. Saglimbeni, and R. Di Leonardo, 2017, *Phys. Rev. X* **7**, 011010.
- Bolitho, A., R. Singh, and R. Adhikari, 2020, *Phys. Rev. Lett.* **124**, 088003.
- Bouvard, J., C. Douarche, P. Mergaert, H. Auradou, and F. Moisy, 2022, *Phys. Rev. E* **106**, 034404.
- Bretherton, F. P., 1962, *J. Fluid Mech.* **14**, 284.
- Brown, A. T., I. D. Vladescu, A. Dawson, T. Vissers, J. Schwarz-Linek, J. S. Lintuvuori, and W. C. K. Poon, 2016, *Soft Matter* **12**, 131.
- Brune, A., P. Frenzel, and H. Cypionka, 2000, *FEMS Microbiol. Rev.* **24**, 691.
- Büschler, K., C. A. Helm, C. Gross, G. Glöckl, E. Romanus, and W. Weitschies, 2004, *Langmuir* **20**, 2435.
- Calovi, D. S., U. Lopez, S. Ngo, C. Sire, H. Chaté, and G. Theraulaz, 2014, *New J. Phys.* **16**, 015026.
- Cates, M. E., and J. Tailleur, 2015, *Annu. Rev. Condens. Matter Phys.* **6**, 219.
- Cavagna, A., and I. Giardina, 2014, *Annu. Rev. Condens. Matter Phys.* **5**, 183.
- Cavagna, A., *et al.*, 2015, *J. Stat. Phys.* **158**, 601.
- Cerdá-Doñate, E., 2020, Ph.D. thesis (University of Potsdam).
- Chattopadhyay, S., R. Moldovan, C. Yeung, and X. L. Wu, 2006, *Proc. Natl. Acad. Sci. U.S.A.* **103**, 13712.
- Chen, C., Q. Ma, W. Jiang, and T. Song, 2011, *Appl. Microbiol. Biotechnol.* **90**, 269.
- Chen, Y.-A., A. D. King, H.-C. Shih, C.-C. Peng, C.-Y. Wu, W.-H. Liao, and Y.-C. Tung, 2011, *Lab Chip* **11**, 3626.
- Chong, W. H., L. K. Chin, R. L. S. Tan, H. Wang, A. Q. Liu, and H. Chen, 2013, *Angew. Chem., Int. Ed.* **52**, 8570.
- Chui, J. Y., C. Douarche, H. Auradou, and R. Juanes, 2021, *Soft Matter* **17**, 7004.
- Clement, E., A. Lindner, C. Douarche, and H. Auradou, 2016, *Eur. Phys. J. Special Topics* **225**, 2389.
- Codutti, A., K. Bente, D. Faivre, and S. Klumpp, 2019, *PLoS Comput. Biol.* **15**, e1007548.
- Codutti, A., M. A. Charsooghi, E. Cerdá-Doñate, H. M. Taïeb, T. Robinson, D. Faivre, and S. Klumpp, 2022, *eLife* **11**, e71527.
- Creppy, A., E. Clément, C. Douarche, M. V. D'Angelo, and H. Auradou, 2019, *Phys. Rev. Fluids* **4**, 013102.
- Creppy, A., F. Plourabou, O. Praud, X. Druart, S. Cazin, H. Yu, and P. Degond, 2016, *J. R. Soc. Interface* **13**, 20160575.
- Darnige, T., N. Figueroa-Morales, P. Bohec, A. Lindner, and E. Clément, 2017, *Rev. Sci. Instrum.* **88**, 055106.
- Dehkharghani, A., N. Waisbord, J. Dunkel, and J. S. Guasto, 2019, *Proc. Natl. Acad. Sci. U.S.A.* **116**, 11119.
- Demirörs, A. F., M. T. Akan, E. Poloni, and André R. Studart, 2018, *Soft Matter* **14**, 4741.
- Dervaux, J., M. C. Resta, and P. Brunet, 2017, *Nat. Phys.* **13**, 306.
- Di Leonardo, R., D. Dell'Arciprete, L. Angelani, and V. Iebba, 2011, *Phys. Rev. Lett.* **106**, 038101.
- Doostmohammadi, A., J. Ignés-Mullol, J. M. Yeomans, and F. Sagués, 2018, *Nat. Commun.* **9**, 3246.
- Drescher, K., J. Dunkel, L. H. Cisneros, S. Ganguly, and R. E. Goldstein, 2011, *Proc. Natl. Acad. Sci. U.S.A.* **108**, 10940.
- Drescher, K., R. E. Goldstein, N. Michel, M. Polin, and I. Tuval, 2010, *Phys. Rev. Lett.* **105**, 168101.
- Elgeti, J., and G. Gompper, 2016, *Eur. Phys. J. Plus* **225**, 2333.
- Erb, R. M., J. J. Martin, R. Soheilian, C. Pan, and J. R. Barber, 2016, *Adv. Funct. Mater.* **26**, 3859.
- Erb, R. M., D. S. Sebba, A. A. Lazarides, and B. B. Yellen, 2008, *J. Appl. Phys.* **103**, 063916.
- Erb, R. M., and B. B. Yellen, 2008, *J. Appl. Phys.* **103**, 07A312.
- Ērglis, K., Q. Wen, V. Ose, A. Zeltins, A. Sharipo, P. A. Janmey, and A. Cēbers, 2007, *Biophys. J.* **93**, 1402.
- Faivre, D., and D. Schüler, 2008, *Chem. Rev.* **108**, 4875.
- Fernández-Gubieda, M. L., L. Marcano, A. Muela, A. García-Prieto, J. Alonso, and I. Orue, 2021, in *New Trends in Nanoparticle Magnetism*, Springer Series in Materials Science Vol. 308, edited by D. Peddis, S. Laureti, and D. Fiorani (Springer, New York), p. 159.
- Fischer, J. P., and H. Cypionka, 2006, *FEMS Microbiol. Ecol.* **55**, 186.
- Frankel, R. B., D. A. Bazylinski, M. S. Johnson, and B. L. Taylor, 1997, *Biophys. J.* **73**, 994.
- Frankel, R. B., R. P. Blakemore, and R. S. Wolfe, 1979, *Science* **203**, 1355.
- Gachelin, J., G. Mino, H. Berthet, A. Lindner, A. Rousselet, and E. Clement, 2013, *Phys. Rev. Lett.* **110**, 268103.
- Gachelin, J., A. Rousselet, A. Lindner, and E. Clement, 2014, *New J. Phys.* **16**, 025003.
- Garcia, X., S. Rafai, and P. Peyla, 2013, *Phys. Rev. Lett.* **110**, 138106.
- Golestanian, R., 2019, *Phys. Rev. E* **100**, 010601.
- Gorby, Y. A., T. J. Beveridge, and R. P. Blakemore, 1988, *J. Bacteriol.* **170**, 834.
- Gotze, I. O., and G. Gompper, 2010, *Europhys. Lett.* **92**, 64003.
- Grant, J., E. Lee, M. Almeida, S. Kim, N. LoGrande, G. Goyal, A. M. Sesay, D. T. Breault, R. Prantil-Baun, and D. E. Ingber, 2022, *Lab Chip* **22**, 1584.
- Grognet, M., and K. M. Taute, 2021, *Curr. Opin. Microbiol.* **61**, 73.
- Grzybowski, B. A., H. A. Stone, and G. M. Whitesides, 2000, *Nature (London)* **405**, 1033.

- Guell, D., H. Brenner, R. B. Frankel, and H. Hartman, 1988, *J. Theor. Biol.* **135**, 525.
- Guzmán-Lastra, F., A. Kaiser, and H. Löwen, 2016, *Nat. Commun.* **7**, 13519.
- Haines, B. M., I. S. Aranson, L. Berlyand, and D. A. Karpeev, 2008, *Phys. Biol.* **5**, 046003.
- Hansen, C. H., R. G. Endres, and N. S. Wingreen, 2008, *PLoS Comput. Biol.* **4**, e1.
- Heywood, B. R., D. A. Bazylinski, A. J. Garratt-Reed, S. Mann, and R. B. Frankel, 1990, *Naturwissenschaften* **77**, 536.
- Hillesdon, A. J., and T. J. Pedley, 1996, *J. Fluid Mech.* **324**, 223.
- Hintsche, M., V. Waljor, R. Großmann, M. J. Kühn, K. M. Thormann, F. Peruani, and C. Beta, 2017, *Sci. Rep.* **7**, 16771.
- Hughes, M. P., and H. Morgan, 1999, *Biotechnol. Prog.* **15**, 245.
- Ilg, P., M. Kroger, and S. Hess, 2002, *J. Chem. Phys.* **116**, 9078.
- Ishikawa, T., T. N. Dang, and E. Lauga, 2022, *Phys. Rev. Fluids* **7**, 093102.
- Jaeger, S., H. Stark, and S. H. Klapp, 2013, *J. Phys. Condens. Matter* **25**, 195104.
- Jana, S., S. G. Charlton, L. E. Eland, J. G. Burgess, A. Wipat, T. P. Curtis, and J. Chen, 2020, *npj Biofilms Microbiomes* **6**, 19.
- Jeffery, G. B., and L. N. G. Filon, 1922, *Proc. R. Soc. A* **102**, 161.
- Jhavar, J., R. G. Morris, U. R. Amith-Kumar, M. D. Raj, T. Rogers, H. Rajendran, and V. Guttal, 2020, *Nat. Phys.* **16**, 488.
- Jibuti, L., L. Qi, C. Misbah, W. Zimmermann, S. Rafai, and P. Peyla, 2014, *Phys. Rev. E* **90**, 063019.
- Jlicher, F., K. Kruse, J. Prost, and J. F. Joanny, 2007, *Phys. Rep.* **449**, 3.
- Jørgensen, B. B., and N. P. Revsbech, 1985, *Limnol. Oceanogr.* **30**, 111.
- Junot, G., N. Figueroa-Morales, T. Darnige, A. Lindner, R. Soto, H. Auradou, and E. Clément, 2019, *Europhys. Lett.* **126**, 44003.
- Keller, E. F., and L. A. Segel, 1971, *J. Theor. Biol.* **30**, 225.
- Klumpp, S., and D. Faivre, 2016, *Eur. Phys. J. Special Topics* **225**, 2173.
- Klumpp, S., C. Lefevre, M. Bennet, and D. Faivre, 2019, *Phys. Rep.* **789**, 1.
- Koch, D. L., and G. Subramanian, 2011, *Annu. Rev. Fluid Mech.* **43**, 637.
- Koessel, F. R., and S. Jabbari-Farouji, 2019, *Europhys. Lett.* **125**, 28001.
- Koessel, F. R., and S. Jabbari-Farouji, 2020, *New J. Phys.* **22**, 103007.
- Kraftmakher, Y., 2007, *Eur. J. Phys.* **28**, 409.
- Kuhn, M. J., F. K. Schmidt, B. Eckhardt, and K. M. Thormann, 2017, *Proc. Natl. Acad. Sci. U.S.A.* **114**, 6340.
- Kumar, A. H., S. J. Thomson, T. R. Powers, and D. M. Harris, 2021, *Phys. Rev. Fluids* **6**, 094501.
- Kumar, M., J. S. Guasto, and A. M. Ardekani, 2022, *J. Rheol.* **66**, 375.
- Kuznetsov, A. V., 2005, *Int. Commun. Heat Mass Transfer* **32**, 991.
- Lauga, E., 2016, *Annu. Rev. Fluid Mech.* **48**, 105.
- Lauga, E., W. R. DiLuzio, G. M. Whitesides, and H. A. Stone, 2006, *Biophys. J.* **90**, 400.
- Lauga, E., and F. Nadal, 2016, *Europhys. Lett.* **116**, 64004.
- Lefèvre, C. T., and D. A. Bazylinski, 2013, *Microbiol. Mol. Biol. Rev.* **77**, 497.
- Lefèvre, C. T., M. Bennet, L. Landau, P. Vach, D. Pignol, D. A. Bazylinski, R. B. Frankel, S. Klumpp, and D. Faivre, 2014, *Biophys. J.* **107**, 527.
- Li, N., C. Luo, X. Zhu, Y. Chen, Q. Ouyang, and L. Zhou, 2011, *Microelectron. Eng.* **88**, 1698.
- Liebchen, B., and D. Levis, 2017, *Phys. Rev. Lett.* **119**, 058002.
- Liebchen, B., and D. Levis, 2022, *Europhys. Lett.* **139**, 67001.
- Lisicki, M., 2013, [arXiv:1312.6231](https://arxiv.org/abs/1312.6231).
- Liu, Z., W. Zeng, X. Ma, and X. Cheng, 2021, *Soft Matter* **17**, 10806.
- Liu, Z., K. Zhang, and X. Cheng, 2019, *Rheol. Acta* **58**, 439.
- Lo, J. F., E. Sinkala, and D. T. Eddington, 2010, *Lab Chip* **10**, 2394.
- López, H. M., J. Gachelin, C. Douarche, H. Auradou, and E. Clément, 2015, *Phys. Rev. Lett.* **115**, 028301.
- Mankiewicz, M., and S. Martel, 2007, in *Optomechatronic Computer-Vision Systems II*, edited by J. Kofman, Y. L. de Meneses, S. Kaneko, C. A. Perez, and D. Coquin, SPIE Proceedings Vol. 6718 (SPIE—International Society for Optical Engineering, Bellingham, WA), pp. 106–114.
- Mann, S., N. H. Sparks, R. B. Frankel, D. A. Bazylinski, and H. W. Jannasch, 1990, *Nature (London)* **343**, 258.
- Manson, M. D., P. Tedesco, H. C. Berg, F. M. Harold, and C. Van der Drift, 1977, *Proc. Natl. Acad. Sci. U.S.A.* **74**, 3060.
- Martinez, V. A., J. Schwarz-Linek, M. Reufer, L. G. Wilson, A. N. Morozov, and W. C. Poon, 2014, *Proc. Natl. Acad. Sci. U.S.A.* **111**, 17771.
- Martínez-Calvo, A., C. Trenado-Yuste, and S. S. Datta, 2021, [arXiv:2108.07011](https://arxiv.org/abs/2108.07011).
- Martiniani, S., P. M. Chaikin, and D. Levine, 2019, *Phys. Rev. X* **9**, 011031.
- Massana-Cid, H., D. Levis, R. J. H. Hernández, I. Pagonabarraga, and P. Tierno, 2021, *Phys. Rev. Res.* **3**, L042021.
- Mathijssen, A. J. T. M., N. Figueroa-Morales, G. Junot, É. Clément, A. Lindner, and A. Zöttl, 2019, *Nat. Commun.* **10**, 3434.
- Matsunaga, D., F. Meng, A. Zöttl, R. Golestanian, and J. M. Yeomans, 2017, *Phys. Rev. Lett.* **119**, 198002.
- Matsunaga, D., A. Zöttl, F. Meng, R. Golestanian, and J. M. Yeomans, 2018, *IMA J. Appl. Math.* **83**, 767.
- McTague, J. P., 1969, *J. Chem. Phys.* **51**, 133.
- Meister, M., 2016, *eLife* **5**, e17210.
- Meng, F., D. Matsunaga, and R. Golestanian, 2018, *Phys. Rev. Lett.* **120**, 188101.
- Meng, F., D. Matsunaga, B. Mahault, and R. Golestanian, 2021, *Phys. Rev. Lett.* **126**, 078001.
- Minagawa, H., Y. Nishikawa, I. Ikeda, K. Miyazaki, N. Takahara, Y. Sakamoto, T. Komai, and H. Narita, 2008, *J. Geophys. Res. Solid Earth* **113**, 07210.
- Morillas, J. R., and J. de Vicente, 2020, *Soft Matter* **16**, 9614.
- Morin, A., D. L. Cardozo, V. Chikkadi, and D. Bartolo, 2017, *Phys. Rev. E* **96**, 042611.
- Murat, D., M. Hrisse, L. Espinosa, A. Bossa, F. Alberto, and L. F. Wu, 2015, *J. Bacteriol.* **197**, 3275.
- Nadkarni, R., S. Barkley, and C. Fradin, 2013, *PLoS One* **8**, e82064.
- Nagard, L. L., L. Yu, M. Rajkotwala, S. Barkley, D. A. Bazylinski, A. P. Hitchcock, and C. Fradin, 2019, *Phys. Biol.* **16**, 066008.
- Nimmo, J. R., 2004, in *Encyclopedia of Soils in the Environment*, edited by D. Hillel (Academic Press, New York), p. 295.
- Odenbach, S., and S. Thurm, 2002, in *Ferrofluids: Magnetically Controllable Fluids and Their Applications*, edited by S. Odenbach (Springer, Berlin), pp. 185–201.
- Park, J., Y. Kim, W. Lee, and S. Lim, 2022, *Sci. Rep.* **12**, 6482.
- Perez, L. J., T. Bhattacharjee, S. S. Datta, R. Parashar, and N. L. Sund, 2021, *Phys. Rev. E* **103**, 012611.
- Perigo, E. A., G. Hemery, O. Sandre, D. Ortega, E. Garaio, F. Plazaola, and F. J. Teran, 2015, *Appl. Phys. Rev.* **2**, 041302.
- Petroff, A., A. Rosselli-Calderon, B. Roque, and P. Kumar, 2022, *Phys. Rev. Fluids* **7**, 053102.
- Petroff, A. P., and A. Libchaber, 2018, *New J. Phys.* **20**, 015007.

- Petroff, A. P., X.-L. Wu, and A. Libchaber, 2015, *Phys. Rev. Lett.* **114**, 158102.
- Pierce, C. J., E. Mumper, E. E. Brown, J. T. Brangham, B. H. Lower, S. K. Lower, F. Y. Yang, and R. Sooryakumar, 2017, *Phys. Rev. E* **95**, 062612.
- Pierce, C. J., E. Osborne, E. Mumper, B. H. Lower, S. K. Lower, and R. Sooryakumar, 2019, *Biophys. J.* **117**, 1250.
- Pierce, C. J., H. Wijesinghe, E. Mumper, B. H. Lower, S. K. Lower, and R. Sooryakumar, 2018, *Phys. Rev. Lett.* **121**, 188001.
- Pierce, C. J., H. Wijesinghe, and E. Osborne, 2020, *AIP Adv.* **10**, 15335.
- Purcell, E. M., 1977, *Am. J. Phys.* **45**, 3.
- Qi, K., E. Westphal, G. Gompper, and R. G. Winkler, 2022, *Commun. Phys.* **5**, 49.
- Raatz, M., M. Hintsche, M. Bahrs, M. Theves, and C. Beta, 2015, *Eur. Phys. J. Special Topics* **224**, 1185.
- Ramamonjy, A., J. Dervaux, and P. Brunet, 2022, *Phys. Rev. Lett.* **128**, 258101.
- Riedel, I. H., K. Kruse, and J. Howard, 2005, *Science* **309**, 300.
- Rismani Yazdi, S., R. Nosrati, C. A. Stevens, D. Vogel, P. L. Davies, and C. Escobedo, 2018, *Small* **14**, 1702982.
- Romanczuk, P., M. Bär, W. Ebeling, B. Lindner, and L. Schimansky-Geier, 2012, *Eur. Phys. J. Special Topics* **202**, 1.
- Ruan, J., T. Kato, C.-L. Santini, T. Miyata, A. Kawamoto, W.-J. Zhang, A. Bernadac, L.-F. Wu, and K. Namba, 2012, *Proc. Natl. Acad. Sci. U.S.A.* **109**, 20643.
- Rupprecht, J. F., N. Waisbord, C. Ybert, C. Cottin-Bizonne, and L. Bocquet, 2016, *Phys. Rev. Lett.* **116**, 168101.
- Saintillan, D., 2010, *Exp. Mech.* **50**, 1275.
- Saintillan, D., 2018, *Annu. Rev. Fluid Mech.* **50**, 563.
- Saintillan, D., and M. J. Shelley, 2012, *J. R. Soc. Interface* **9**, 571.
- Sanoria, M., R. Chelakkot, and A. Nandi, 2022, *Phys. Rev. E* **106**, 034605.
- Saragosti, J., P. Silberzan, and A. Buguin, 2012, *PLoS One* **7**, 1.
- Schulz-Vogt, H. N., *et al.*, 2019, *ISME J.* **13**, 1198.
- Secchi, E., A. Vitale, G. L. Miño, V. Kantsler, L. Eberl, R. Rusconi, and R. Stocker, 2020, *Nat. Commun.* **11**, 2851.
- Sengupta, A., 2022, *Physics* **15**, 88.
- Singh, R., and R. Adhikari, 2016, *Phys. Rev. Lett.* **117**, 228002.
- Singh, R., and R. Adhikari, 2019, [arXiv:1910.00909](https://arxiv.org/abs/1910.00909).
- Sip, C. G., N. Bhattacharjee, and A. Folch, 2011, *Biomicrofluidics* **5**, 022210.
- Sipos, O., K. Nagy, R. Di Leonardo, and P. Galajda, 2015, *Phys. Rev. Lett.* **114**, 258104.
- Smyk, S., V. Telezki, J. R. Lett, J. Hayes, and S. Klumpp, 2021, *Eur. Phys. J. Special Topics* **230**, 1099.
- Snezhko, A., 2016, *Curr. Opin. Colloid Interface Sci.* **21**, 65.
- Snezhko, A., and I. S. Aranson, 2011, *Nat. Mater.* **10**, 698.
- Snezhko, A., I. S. Aranson, and W.-K. Kwok, 2006, *Phys. Rev. E* **73**, 041306.
- Sokolov, A., and I. S. Aranson, 2016, *Nat. Commun.* **7**, 11114.
- Son, K., J. S. Guasto, and R. Stocker, 2013, *Nat. Phys.* **9**, 494.
- Sosa-Hernández, J. E., M. Santillán, and J. Santana-Solano, 2017, *Phys. Rev. E* **95**, 032404.
- Stock, J., and M. Baker, 2009, in *Encyclopedia of Microbiology*, edited by M. Schaechter (Elsevier, New York), pp. 71–78.
- Stocker, R., 2011, *Proc. Natl. Acad. Sci. U.S.A.* **108**, 2635.
- Stricker, L., I. Guido, T. Breithaupt, M. G. Mazza, and J. Vollmer, 2020, *J. R. Soc. Interface* **17**, 20200559.
- Taukulis, R., and A. Cebers, 2014, *J. Magn. Magn. Mater.* **368**, 428.
- Tay, A., D. Pfeiffer, K. Rowe, A. Tannenbaum, F. Popp, R. Strangeway, D. Schler, and D. D. Carlo, 2018, *Appl. Environ. Microbiol.* **84**, e01308, <https://journals.asm.org/doi/pdf/10.1128/aem.01308-18>.
- Taylor, G. I., 1953, *Proc. R. Soc. A* **219**, 186.
- Théry, A., L. L. Nagard, J. C. Ono-dit-Biot, C. Fradin, K. Dalnoki-Veress, and E. Lauga, 2020, *Sci. Rep.* **10**, 13578.
- Thutupalli, S., D. Geyer, R. Singh, R. Adhikari, and H. A. Stone, 2018, *Proc. Natl. Acad. Sci. U.S.A.* **115**, 5403.
- Uday Bhaskar, R., R. Karmakar, D. Deepika, M. S. Tirumkudulu, and K. Venkatesh, 2015, *Syst. Synth. Biol.* **9**, 85.
- Uhlenbeck, G. E., and L. S. Ornstein, 1930, *Phys. Rev.* **36**, 823.
- Vach, P. J., D. Walker, P. Fischer, P. Fratzl, and D. Faivre, 2017, *J. Phys. D* **50**, 11LT03.
- Vicsek, T., and A. Zafeiris, 2012, *Phys. Rep.* **517**, 71.
- Vincenti, B., 2019, Ph.D. thesis (Sorbonne University).
- Vincenti, B., C. Douarche, and E. Clement, 2018, *Phys. Rev. Fluids* **3**, 033302.
- Waisbord, N., A. Dehkharghani, and J. S. Guasto, 2021, *Nat. Commun.* **12**, 5949.
- Waisbord, N., C. Lefèvre, L. Bocquet, C. Ybert, and C. Cottin-Bizonne, 2016a, *Phys. Rev. Fluids* **1**, 053203.
- Waisbord, N., C. Lefèvre, L. Bocquet, C. Ybert, and C. Cottin-Bizonne, 2016b, [arXiv.1603.00490](https://arxiv.org/abs/1603.00490).
- Wang, B., Z. Rozynek, J. O. Fossum, L. F. Chiara, M. E. Rosti, F. Picanoal, H. Behmadi, Z. Fazli, A. Najafi, and A. Najafi, 2018, *J. Stat. Mech. Theory Exp.* **2018**, 023201.
- Wang, M., L. He, and Y. Yin, 2013, *Mater. Today* **16**, 110.
- Wensink, H. H., J. Dunkel, S. Heidenreich, K. Drescher, R. E. Goldstein, H. Lwen, and J. M. Yeomans, 2012, *Proc. Natl. Acad. Sci. U.S.A.* **109**, 14308.
- Wioland, H., E. Lushi, and R. E. Goldstein, 2016, *New J. Phys.* **18**, 075002.
- Xue, R., Q. Ma, M. A. B. Baker, and F. Bai, 2015, *Adv. Sci.* **2**, 1500129.
- Yan, J., S. C. Bae, and S. Granick, 2015, *Soft Matter* **11**, 147.
- Yazdi, S. R., R. Nosrati, C. A. Stevens, D. Vogel, and C. Escobedo, 2018, *Biomicrofluidics* **12**, 011101.
- Yu, L., L. Le Nagard, S. Barkley, L. Smith, and C. Fradin, 2022, *Phys. Rev. E* **106**, 034407.
- Zhang, W.-J., and L.-F. Wu, 2020, *Biomolecules* **10**, 460.
- Zöttl, A., and H. Stark, 2012, *Phys. Rev. Lett.* **108**, 218104.